Colloid-Facilitated Radionuclide Transport in Fractured Carbonate Rock from Yucca Flat, Nevada National Security Site

M. Zavarin, S.K. Roberts, M.R. Johnson, Q. Hu, B.A. Powell, P. Zhao, A.B. Kersting, R.E. Lindvall, R.J. Pletcher

February 19, 2013

Disclaimer

This document was prepared as an account of work sponsored by an agency of the United States government. Neither the United States government nor Lawrence Livermore National Security, LLC, nor any of their employees makes any warranty, expressed or implied, or assumes any legal liability or responsibility for the accuracy, completeness, or usefulness of any information, apparatus, product, or process disclosed, or represents that its use would not infringe privately owned rights. Reference herein to any specific commercial product, process, or service by trade name, trademark, manufacturer, or otherwise does not necessarily constitute or imply its endorsement, recommendation, or favoring by the United States government or Lawrence Livermore National Security, LLC. The views and opinions of authors expressed herein do not necessarily state or reflect those of the United States government or Lawrence Livermore National Security, LLC, and shall not be used for advertising or product endorsement purposes.

Colloid-Facilitated Radionuclide Transport in Fractured Carbonate Rock from Yucca Flat, Nevada National Security Site

Mavrik Zavarin[1], Sarah K. Roberts[2], Mackenzie R. Johnson[3],
Qinhong Hu[1], Brian A. Powell[1], Pihong Zhao[1], Annie B. Kersting[1], Rachel E. Lindvall[1], and
Ronald J. Pletcher[2]

[1]Chemistry, Materials, and Life Sciences Directorate*

[2]Energy and Environment Directorate*

[3]Engineering Directorate*

Lawrence Livermore National Laboratory

Livermore, California

May, 2013

* Directorates are identified as they existed when experiments were conducted (2006).

TABLE OF CONTENTS

LIST OF FIGURES

LIST OF TABLES

1   INTRODUCTION

In the Yucca Flat basin of the Nevada National Security Site (NNSS), ~750 nuclear detonations were conducted, primarily within the tuff confining unit (TCU) and the overlying alluvium. The regional carbonate aquifer (lower carbonate aquifer) is located below the TCU and is the most likely pathway for radionuclide migration off the NNSS. The regional carbonate aquifer underlies most of the NNSS and is known to be highly transmissive. Two principal pathways for LCA contamination exist in Yucca Flat. The first is composed of shortcuts (e.g. fractures) through the TCU which may provide a radionuclide transport pathway from tests conducted in the overlying alluvium and volcanics. The second is the release and migration of radionuclides from a small number (four) of tests conducted directly in the carbonate rock. Two of those tests were located near the saturated zone (Nash and Bourbon).

Understanding the migration behavior of radionuclides once they reach the fractured LCA is the subject of this report. Because the LCA is the regional aquifer unit and a potentially important radionuclide transport pathway, in FY2005, LLNL conducted a set of laboratory experiments to examine radionuclide transport in carbonate fractures (Zavarin et al., 2005). A complimentary experimental effort was conducted by LANL (Ware et al., 2005) and a summary report has been issued (Zavarin et al., 2006). Absent from these experiments was an examination of the role of colloids in radionuclide transport in carbonate rock. This report summarizes experiments that evaluated the role of colloids in radionuclide transport in fractured carbonate rock. Colloid-facilitated transport has be identified as an important transport mechanisms in fractured tuff (Kersting et al., 1999). It is likely to be similarly important in fractured carbonate.

Carbonate cores were prepared from archived ER-6-1 core obtained from the USGS Core Library, Mercury, Nevada. The core was originally collected in 1994 and placed in boxes without any attempt to preserve natural water contents. Flowthrough experiments were performed using smooth parallel-plate fractures synthesized from the solid core. Smooth parallel-plate fractures were used to better control the processes affecting transport. Natural fractures contain variable apertures and heterogeneously distributed fracture lining minerals which complicate data interpretation. Previous data have shown that transport behavior observed in synthetic parallel-plate fractures is comparable to natural fractures; differences can be attributed largely to the role of fracture lining minerals. Parallel-plate (slotted) fractures were synthesized with apertures of 500 and 50 micrometers. The transport of non-sorbing ^{3}H and Re(VII), and sorbing Sm(III), U(VI), Pu(IV), and Pu(V) was examined by introducing a short pulse of tracers into the synthetic fracture at a constant flow rate and measuring their breakthrough (i.e. a flowthrough experiment). The tracers ^{3}H and ReO_4^- are non-sorbing; their transport behavior will be controlled by their diffusivity from the fracture into the carbonate matrix. Samarium(III) is expected to sorb very strongly to both colloids and the carbonate matrix; its transport will be governed by colloid-facilitated transport. Samarium behaves similar to other trivalent radionuclides that have been deposited in the subsurface of the NNSS as a result of underground nuclear testing. (e.g. ^{244}Cm, ^{243}Am, ^{241}Am, ^{150}Eu, ^{152}Eu, ^{154}Eu, ^{166}Ho). Uranium(VI) sorption to aluminosilicate colloids and carbonate rock is weak. It is expected to migrate as an aqueous species and only slightly retarded by its interaction with the carbonate

matrix. Plutonium(IV) is expected to sorb strongly to both colloids and the carbonate matrix. However, as Pu(V), plutonium is a weak sorber and may migrate as an aqueous species.

During the flowthrough experiments, radionuclide concentrations in the effluent were measured. At the conclusion of the experiments, the distribution of radioactive components that were not transported entirely through the column was examined using autoradiography and laser ablation inductively coupled plasma mass spectrometry (LA/ICP-MS). These data were used to evaluate the accessibility of the rock matrix to tracer diffusion and sorption. At the conclusion of all effluent and post-test core analyses, the reactive transport of radionuclides in the fractures was modeled. Data were modeled using the CRUNCH code (Steefel and Yabusaki, 1995) combined with our surface complexation and ion exchange sorption database (Zavarin and Bruton, 2004a; Zavarin and Bruton, 2004b). Data were also modeled using the RELAP (REactive transport LAPlace transform inversion computer code) code. This code solves a semi-analytical dual-porosity transport model of fracture transport. RELAP is described in detail in Reimus and Haga, (1999), Reimus et al. (2003), and Reimus et al. (2002). RELAP/RETRAN solves Laplace transformed versions of the 1-D dual-porosity transport equations using a Laplace-to-time domain inversion algorithm. One of the solutions included in the RELAP model is the parallel plate, infinite matrix, equilibrium sorption fracture transport solution of Tang et al. (1981). However, RELAP/RETRAN may also account for finite matrices, rate-limited sorption, and radial flow. All data and modeling results are compared to earlier carbonate fracture transport experiments in the absence of colloids.

2 FRACTURE TRANSPORT METHODS

2.1 Core Preparation

Fracture flowthrough experiment core characteristics are listed in Table 2.1. The carbonate cores had an original diameter of 83 mm (3.25 inches) and were sub-cored to a diameter of 70 mm using a diamond impregnated water-cooled core barrel. The ends of each core were ground with a precision grinding machine to the size designated for each of the two flowthrough reactors. The Appendix contains photographs of the prepared cores used in the flowthrough tests.

Table 2.1 Core parameters.

Exp#	Well and depth	Mass	Length	Diam	Aperture	Porosity	Permeability	Bulk Density	Inflow Tube Vol.	Outflow Tube Vol.	Flow Rate
	feet	g	mm	mm	μm	%	md[1]	g/cm^3	mL	mL	mL/min
LCA-5	ER-6-1 2601.7-2602.8	1204	113	70	500	1.0	1.9E-3	2.80	1.42	0.59	0.02
LCA-6	ER-6-1 2619.0-2620.0	~1200	128	70	50	4.9	6.0	2.70	1.84	0.68	0.02

[1] Units of permeability are presented as millidarcy (md). 1 Darcy = 9.87×10^{-13} m^2.

The subcores were sawed in half and opposing faces of the core were ground flat and parallel to the saw-cut (used for orientation purposes during grinding). The two inner faces were then ground flat with a fine-grained diamond impregnated grinding wheel. The same machine was used to grind a trench in one of the surfaces such that when the two halves were re-joined, there

would be a synthetic fracture (a "slot") with a known aperture with a width equal to the depth of the trench (see Figures 2.1 and 2.2). The depth of this trench was 500 and 50 μm for LCA-5 and LCA-6, respectively. After both ends of the core had been ground flat (and thus perpendicular to the length of the core), the halves were placed in an ultrasonic bath of deionized water for five minutes to remove any fine-grained particles from the pores that were trapped during the machining. The cores were then placed in a 50°C oven for 48 hours. Finally, the two halves were glued together by applying Devcon® Flexane quick-drying, chemically-resistant rubber epoxy to the external edges of the synthetic fracture. The cores were then placed in a flowthrough apparatus.

2.2   Core Characteristics

The porosity, density, and permeability of each core are reported in Table 2.1. Measurements were made by sub-coring one inch diameter (2.54 cm) plugs from rock adjacent vertically to the prepared fractured cores and shipping the plugs to Core Laboratories Inc. (Aurora, CO) for analysis. Specific physical properties (length, diameter, weight, and bulk volume) of each plug sample were measured and recorded. Samples were dried in an oven for 24 hours at 180°F (80°C) before permeability and porosity measurements were recorded. Permeability (using nitrogen) and porosity (using helium) were measured for each sample according to standard procedures (API RP 27, 1952; API RP 40, 1960).

For porosity, samples were placed into a Coberly-Stevens Boyle's Law porosimeter and injected with helium at approximately 100 psig. Corresponding pressures and volumes were measured and Boyle's Law was used to calculate sample grain volume. Pore volume was determined by subtracting the calculated grain volume from the measured bulk volume. Grain density and bulk density values were calculated from these measurements. Importantly, rock porosities can vary substantially over very short distances. Thus, the reported porosities may not be equivalent to those of the synthetically fractured cores used in flowthrough experiments. Nevertheless, it is quite clear that the porosity of these rocks is quite low.

For permeability, samples were placed into a Hassler-Sleeve core holder. The annulus of the core holder was pressurized to a pre-determined value (400 psig minimum) to seal the sample. Nitrogen gas was forced through the sample at a given pressure under steady-state conditions. The flow rate was measured and permeability to air was calculated. A Klinkenberg-corrected permeability value was obtained using these values.

The mineralogy of the carbonate cores was determined by x-ray diffraction (XRD). X-ray scans were collected using a Scintag PAD-V generator equipped with a Cu x-ray tube operated at 45 kV and 35 mA, and a Sieffert goniometer with a solid-state detector. Diffraction patterns were collected in step scan mode at 4 seconds per 0.02° 2θ. Collimation was provide by a 1° divergence and 2° scatter slit on the x-ray tube and a 0.3 mm scatter and 0.2 mm registration slit on the detector. Samples were scanned from 2 to 72° 2θ.

Quantitative mineralogic analyses were performed using the Rietveld method. Phase identification was accomplished using an XRD pattern processing software program (Jade, version 3.0, Materials Data, Inc., Livermore, CA), which utilizes data from the Joint Committee

on Powder Diffraction Standards Powder Diffraction File (JCPDS-PDF). The Rietveld least squares refinement was performed using a quantitative XRD software program (Siroquant, version 2.0, Sietronics, Australia). Both cores were composed of essentially pure dolomite. Quartz was the only other mineral identified in LCA-5 at 1.6%.

2.3   Solution Composition

The background solution composition used in the carbonate flowthrough experiments (Table 2.2) was based on measured concentrations of major ions in groundwaters sampled from the LCA (Table 2.3), culled from the UGTA geochemistry database (Stoller-Navarro, 2004). Sulfate, nitrate, and fluoride were omitted from the background solution because their role in radionuclide retardation is expected to be minimal. The calcium concentration was adjusted by equilibrating background solutions with calcite to minimize calcite dissolution/precipitation during flowthrough experiments. The LCA experiment solution was prepared at equilibrium with atmospheric $CO_2(g)$ (higher pH and lower carbonate alkalinity than measured LCA groundwater composition) to improve solution composition stability. Sensitivity calculations suggest that the difference in groundwater composition may increase the experiment Kd by as much as 0.5 log units for Pu but significantly less for other radionuclides when compared to average LCA groundwater chemistry.

Table 2.2 Composition of background solutions used in flowthrough experiments.

Exp#	pH	Na	Mg	K	Ca
		-------------------- mol/L --------------------			
LCA-5	7.9	4.1×10^{-3}	9.1×10^{-4}	4.5×10^{-4}	7.7×10^{-4}
LCA-6	7.8	3.8×10^{-3}	8.8×10^{-4}	2.3×10^{-3}	8.6×10^{-4}

Radionuclides used in the flowthrough experiments were chosen because they represent a range of transport behavior. Table 2.4 summarizes the radionuclide composition of these solutions. The solutions were prepared by spiking the prepared background solutions with the appropriate amount of each radionuclide. The concentration of each radionuclide was chosen based on a combination of instrument detection limits, expected background concentrations in equilibrium with LCA rock, solubility limits, and sorption linearity.

For Pu, two stock solutions were used to provide an appropriate [238]Pu alpha signal for Liquid Scintillation Counting (LSC) and post-test characterization and [242]Pu signal for ICP-MS analysis. Both Pu stock solutions were purified using TEVA resin (Eichrom Technologies, Inc.) columns and diluted into 1 mol/L HNO_3.

4

Table 2.3 Composition of LCA waters in Yucca Flat.

SITE_ID	Sample Date	Water Temp °C	pH	Ca	Mg	Na	K	^{1}HCO$_3$	Cl	SO$_4$	NO$_3$	F
				----------------------------- mg/L -----------------------------								
USGS Water Well C	9/11/1990	36	7.3	74.5	28.2	126	13.2	584	33.2	65	n.d.	1.1
Water Well C-1	9/25/1996	37	6.7	73	27	120	14	580	33	66	n.d.	1.1
ER-6-1	10/9/1992	43.7	7.87	33.4	12.2	47	8.32	237	11.8	32.1	0.58	0.68
ER-6-1 #2	1/16/2003	39.9	7.6	33.6	14	47.1	6.3	256	10	34	1.1	0.8
ER-3-1	10/16/1996	37.8	6.69	94.9	35.1	143	19	741	43.4	68.1	<0.05	1.38
U-3cn #5	1/29/1997	42.4	7.21	39.6	16.7	53.4	7.9	262	29.5	36.2	<0.05	0.87
UE-1h (651 m depth)	5/26/1993	25.3	8.2	15.3	7.5	102	25	276	43.6	25	n.d.	0.7
UE-1c	8/31/1988	26	7.98	34.1	13.2	33.7	12.7	238	6.7	34.1	2.4	0.5
UE-1q	7/10/1992	31.5	7.8	29.4	15.3	31.2	4.6	199	5.3	n.d.	n.d.	n.d.
UE-10j (765-773 m depth)	3/17/1997	32.7	6.43	101	42.3	64	12.3	504	24	83	n.d.	0.3
UE-10j (732-740 m depth)	3/20/1997	32.3	6.73	68	30	43	8.3	403	16	67	n.d.	0.3
UE-10j (691-699 m depth)	3/24/1997	32.1	6.96	56	25.4	35	6.9	349	12.5	60.8	n.d.	0.3
Average			7.3	51	21	60	11	368	20	49	<1.4	0.7
Standard deviation			0.6	29	11	36	6	173	14	21		0.4
				----------------------------- mol/L -----------------------------								
Average				1.3E-3	8.7E-4	2.6E-3	2.8E-4	6.0E-3	5.7E-4	5.1E-4	<2.2E-5	3.8E-5
Standard Deviation				7.2E-4	4.7E-4	1.6E-3	1.6E-4	2.8E-3	4.0E-4	2.2E-4		1.9E-5

[1] Total carbonate in solution reported as mol/L of HCO$_3^-$.

Table 2.4 Radionuclide composition of solutions used in flowthrough experiments.

Sample #	^{3}H cnts/min	Sm	Re	U	^{242}Pu stock[a]	^{238}Pu stock[a]
		-------------------------- mol/L --------------------------				
LCA-5	3.88×10^2	9.28×10^{-7}	1.01×10^{-6}	5.04×10^{-6}	1.96×10^{-9}	3.0×10^{-9}
LCA-6	3.60×10^2	7.22×10^{-7}	1.03×10^{-6}	9.74×10^{-7}	2.11×10^{-9}	3.0×10^{-9}

[a] Concentrations refer to the total Pu concentration in these stock solutions and not the concentration of any particular isotope. See text for the percentages of ^{238}Pu, ^{239}Pu, ^{240}Pu, ^{241}Pu, and ^{242}Pu in the stock solution

The first Pu stock solution (referred to as Pu-242 stock) contained 0.0098% ^{238}Pu, 0.0040% ^{239}Pu, 0.104% ^{240}Pu, 0.047% ^{241}Pu, and 99.84% ^{242}Pu by mass. The stock Pu was reduced to Pu(IV) and the oxidation state tested using a Guided Wave Model 260 Fiber Optic spectrophotometer. However, Pu(IV) is inherently unstable in this solution and oxidized with time. At the start of the experiments, the solution was ~40% Pu(V/VI) and ~60% Pu(IV).

The isotopic contents of the second Pu stock solution (referred as Pu-238 stock) were 7.03% ^{238}Pu, 87.19% ^{239}Pu, 5.57% ^{240}Pu, 0.15% ^{241}Pu and 0.05% ^{242}Pu by mass as determined by α-spectrometry. The stock Pu was reduced to Pu(IV) and the oxidation state confirmed using solvent extraction with 4-Benzoyl-3-methyl-1-phenyl-2-pyrozolln-5-one (PMBP). The extraction results showed that >90±5% was Pu(IV). As in the other stock solution, by the start of the experiments, a significant fraction of the Pu had reoxidized; the starting solution was ~95% Pu(V/VI) and ~5% Pu(IV).

It should be noted that the stability of Pu(IV) in solution increases in the presence of sorbing mineral surfaces (e.g. colloids). Thus, when stock solutions were added to the colloid-containing sorption solutions, it is likely that some of the Pu(V/VI) began slowly reducing to Pu(IV). Thus, the oxidation state of Pu in the stock solutions is not likely to be a very accurate representation of the oxidation state of the sorption solution over time.

Of the radionuclides included in the sorption solution, ^{3}H and ReO_4^- will behave as non-sorbing tracers. The only difference in their transport behavior will result from the lower diffusivity of ReO_4^- and possible charge exclusion effects due to the negative charge on the ReO_4^- anion. At 25°C, the diffusivity of ReO_4^- in water is significantly less than that of ^{3}H (1.5×10^{-9} (Lide, 2000) and 2.2×10^{-9} m^2/sec (Mills, 1973), respectively). The tracer ReO_4^- was used as an analog to TcO_4^-. Divergence in the breakthrough profile of these two non-sorbing tracers is an indication that matrix diffusion is occurring.

The Sm(III), U(VI), and Pu radionuclides can form a variety of aqueous complexes with CO_3^{2-}, OH$^-$, or both under the experimental solution conditions. Sm(III) will complex with CO_3^{2-} to form $SmCO_3^+$ and $Sm(CO_3)_2^-$ at our experimental solution conditions. The formation of $Sm(CO_3)_2^-$ will tend to reduce sorption because the negative charge of most mineral surfaces at pH ~8.5 will result in electrostatic repulsion. Nevertheless, the strong affinity of Sm for most mineral surfaces is expected to result in minimal Sm transport in carbonate fractures in the absence of colloids (Zavarin et al., 2005). Pu(IV) is expected to be in solution as the hydroxide complex, $Pu(OH)_4^0$, and as the hydroxycarbonate complex, $Pu(OH)_2(CO_3)_2^{2-}$. As for other radionuclides, the formation of negatively-charged aqueous species will tend to reduce sorption. This was observed in sorption experiments reported in (Kersting et al., 2003). Nevertheless, Pu(IV) expresses a moderate affinity for calcite surfaces and aluminosilicate colloids. Unlike Pu(IV), Pu(V) sorption to both calcite and aluminosilicate surfaces is quite weak (Zavarin and Bruton, 2004b; Zavarin et al., 2005). Thus, the transport behavior of Pu will be controlled in large part, by the oxidation state speciation of Pu in groundwater. This will become quite evident in the flowthrough experiments described below.

2.4 Colloid Characteristics

Both LLNL and LANL have investigated radionuclide transport in fractured carbonate core (Ware et al., 2005; Zavarin et al., 2005; Zavarin et al., 2006). However, those experiments did not (intentionally) examine the role of colloids in facilitating radionuclide transport in the LCA. To examine the role of colloids, column experiments were prepared so as to achieve a steady-state colloid load in the fracture fluid. This is expected to be representative of field conditions where colloid generation and filtration rates have likely reached steady state. To achieve steady-state conditions, the radionuclide sorption cocktail and the background solution for each experiment included colloids. Prior to injection of radionuclides, sufficient background colloid-containing solution was injected to reach a steady state colloid load in the fracture fluid. For the LCA-5 experiment, the heulandite colloid concentration in the column in-flow and out-flow was 63.2 and 63.1 mg/L, respectively. In LCA-6, a steady state silica colloid load of 1000 mg/L was used. These colloid concentrations are substantially higher that observed in the field. Thus, their filtration behavior may be an artifact that is not representative of field conditions. As a result, caution needs to be exercised when extrapolating these results directly into a field transport

model. Nevertheless, these colloid facilitated transport experiments are intended to provide qualitative insight into the potential colloid-facilitated transport of certain radionuclides in fractured carbonate rock.

For LCA-5, 63 mg/L colloidal heulandite (153 nm average particle size) was used[1]. The heulandite particles were the product of pulverizing a single heulandite crystal in an agate mortar and pestle followed by particle size segregation using centrifugation. Initial examination of LCA-5 column breakthrough indicated that less Pu was recovered than expected. The fraction of ^{238}Pu sorbed onto the colloids in the spike solution was analyzed and found to be relatively small (Table 2.5), most likely due the oxidized state of Pu in solution. For LCA-6, very high surface area silica colloids were used to increase Pu association with colloids. The silica colloids were obtained by washing a commercial colloidal silica solution (Ludox HS-30) to remove excess sodium. The 22.4 nm silica colloids sorbed >99 percent of the ^{238}Pu when a colloid load of 1000 mg/L was used. Sorption was measured in the spike solution prior to injections by centrifugation and scintillation counting.

Table 2.5 Percentage of Pu associated with colloids.[a]

	Analysis date	^{238}Pu
LCA-5 (with zeolite colloids)	5/5/06	14%
LCA-6 (with silica colloids)	7/25/06	99%

[a] Only the association of ^{238}Pu with colloids was measured. The association of ^{242}Pu with colloids is not known.

2.5   Flowthrough Experiment Apparatus

An existing flowthrough reactor was used to perform the transport experiments. A photograph of the core apparatus is shown in Figure 2.1, and a schematic of the apparatus is shown in Figure 2.2. The core is sealed on the outside with flexible tubular membranes. The entire core is subjected to external pressure to squeeze the membrane against the outside of the core to prevent fluid flow along the core wall. Water was used as the confining pressure medium and was controlled by a gradient HPLC pump (Gilson 305) at a flow rate that produced a constant pressure of 10 PSI. Fluid flow through the core was also controlled by a gradient HPLC pump (Gilson 305) set to a rate of 0.02 mL/min.

---

[1] All reported colloid sizes were measured using a Brookhaven Instruments, Inc., particle size analyzer which uses the principles of dynamic light scattering to estimate particle size.

Figure 2.1 Photograph of experimental set-up showing membrane sealed core in flowthrough reactor. Gradient HPLC pump that controlled flow rate is behind the flowthrough reactor, and the fraction collector for outflow solutions is seen at right.
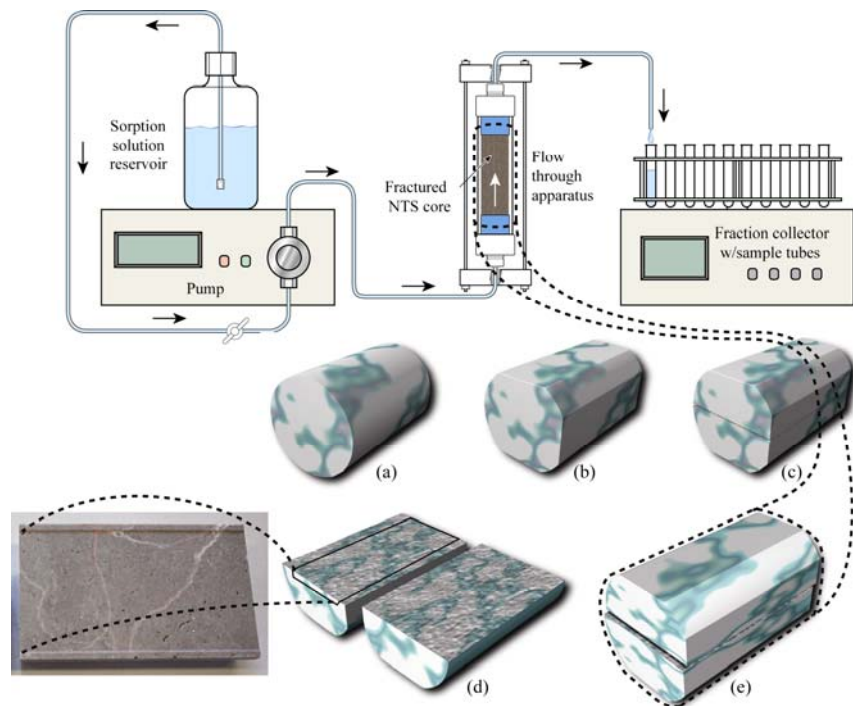
Figure 2.2 Fracture flow experiment diagram where sketches (a) to (e) show steps in experiment preparation (slotted fractures). Sample core (a) has reference flats ground on end surfaces and at relative azimuths of 0, 90, and 180° on the cylindrical surface (b); core is cut in half (c); is laid open and a 500 or 50 μm wide slot is ground into one side (d); finally it is reassembled (e) for experiments. (Images (a)-(e) from Durham et al. (2001)).

2.6 Flowthrough Experiment Procedure

Each of the flowthrough experiments occurred in four steps: a $CO_{2\,(g)}$ flush, core saturation (initially without colloids, then with colloids), a sorption pulse, and a desorption stage. Table 2.6 provides a summary of the stage durations for each experiment.

Table 2.6 Duration (in days) of each experimental stage for the individual cores.

	LCA-5	LCA-6
$CO_{2\,(g)}$	1.08	0.71
Core Saturation	6.00	13.20
Sorption	0.66	0.71
Desorption	8.98	9.11

To ensure full saturation of the core, it was necessary to remove air from the core. One method used to ensure core saturation is to apply a vacuum to the core followed by introduction of water. Alternatively, carbon dioxide can be flushed through the core. Unlike the air it replaces, $CO_{2\,(g)}$ will readily dissolve in water. As the $CO_{2\,(g)}$ dissolves, it is replaced by the water that is introduced into the core. For the present set of experiments, $CO_{2\,(g)}$ was pumped through the core overnight.

After the $CO_{2\,(g)}$ flush, a background solution was pumped through the core for a period of 6 to 13 days. Flushing the core with background solution provided reasonable confidence that the core was fully saturated, the $CO_{2\,(g)}$ had dissolved, and the core was at equilibrium with the background solution prior to the addition of radionuclides.

The sorption solution pulse was typically pumped through the core for 16 to 17 hours. Data collection began simultaneously with the introduction of the sorption solution, and continued for a period lasting up to 10 days to capture the effects of desorption and diffusion. The sorption pulse is delineated by the vertical black lines on the breakthrough plots that are presented in Sections 3.1 and 3.2.

2.7 Effluent and Post-Test Core Characterization

Effluent U, Pu, Re, and Sm concentration were analyzed on either a Agilent HP4500 ICP-MS or a Thermo X7 ICP-MS. Major cations (Na, Ca, K, and Mg) were measured on the ICP-MS as well. Typically, samples were diluted 100 times with 2% nitric acid; an internal standard was always included. A Tri-Carb 2500 Liquid Scintillation analyzer from Packard Instrument Company was used for liquid scintillation counting of ^{238}Pu and ^{3}H. Following the flowthrough experiments, α-radiography and LA/ICP-MS were used to determine the location of radionuclides in the cores.

Alpha-radiography is an in-situ, non-destructive technique based upon the decay properties of α-emitting radionuclides to visualize their spatial distribution. Plutonium isotopes used in the flowthrough experiments are α-emitters, and hence can be detected by using CR-39 film, a polymer of polyallyl diglycol carbonate plastic produced by Track Analysis Systems, Ltd. in Bristol, U.K. The film has a high sensitivity toward 1 MeV protons, 6 MeV α-emissions, and an excellent optical quality making it ideal for identification of nuclear material (Cartwright et al., 1978). For these experiments, 100mm x 100mm pieces of the CR-39 film were placed in direct contact with the flat core surface. The film was exposed to the LCA-5 and LCA-6 cores for 4 and 5 days, respectively. During the exposure process, α particles are released from their source on the core and strike the film, forming an indentation. Following exposure, the α-tracks were etched by heating the plates for 5 hours at $75^{\circ}C$ in a 6.3 N NaOH solution. The plates were scanned using a Mictrotek Scanmaker i700 digital scanner. One radiography plate was left on the benchtop near the core as a positive control and no significant α-tracks were observed. Specific regions of each core were inspected using an optical microscope equipped with a digital camera (Polaroid Model DMC 1 digital camera and Wild Makroskop M420 microscope).

Laser ablation refers to the process in which an intense burst of energy delivered by short laser pulses is used to vaporize a minute (in the range of nanograms) sample from a specific location. The chemical composition of the vaporized sample is then analyzed by ICP-MS. Since 1985, LA/ICP–MS has evolved as a powerful analytical tool for *solid* sampling and analysis (e.g., (Russo et al., 2000; Russo et al., 2002). LA/ICP–MS can determine simultaneously a large number of chemical elements at low detection limits, typically in the range of nanograms to low-micrograms per gram.

We used a laser ablation system (CETAC LSX-200, CETAC Technologies, Omaha, NE), with spot-size options ranging from 10 μm to 300 μm, interfaced with an ICP-MS (X-Series ICP-MS, Thermo Electron Corporation, West Palm Beach, FL). During data acquisition, signal intensities (counts per second, cps) were recorded for a number of elements, including introduced chemicals/radionuclides (^{147}Sm, ^{185}Re, ^{238}U, and ^{242}Pu) and other elements intrinsic to the rock (e.g., ^{26}Mg, ^{44}Ca, ^{85}Rb). Examples of signal response from LA/ICP-MS are shown in Figure 2.3; about 10 seconds after ablation from laser firing, elements are detected by the ICP-MS. Signal intensity in the y-axis indicates the signal response measured by the ICP-MS for the laser-ablated mass. The signal intensity measured during the initial 10 second period is used to determine the instrument background for each element. When the sample reaches the detector, there is a sharp rise in signal intensity, followed by a gradual decrease in intensity to near-background levels within several minutes after laser firing. After the background is subtracted from the sample signal, integrating under the curve provides the sample signal intensity. Differences in the integrated signal intensity for different elements reflect their differences in concentration in the sample matrix.
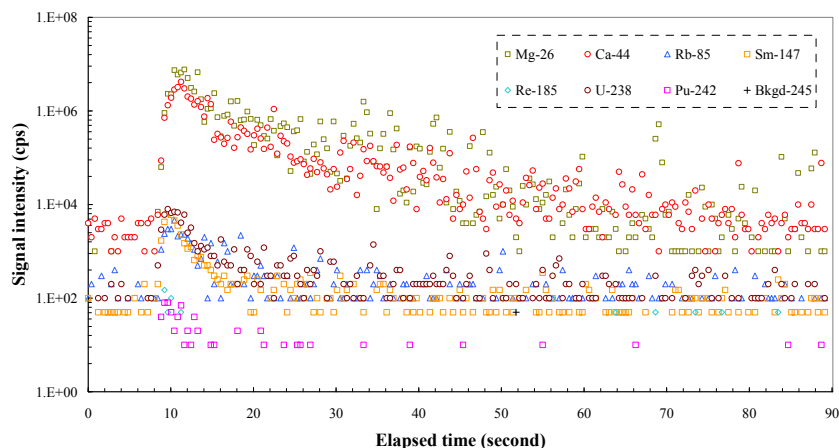
Figure 2.3 Examples of signal responses for elements from laser ablation on the LCA-6 sample. "Bkgd" represents instrument background.

We have adopted a robust method to monitor and correct the ICP-MS instrumental drift during a run period, by continuously sampling a 5 ppb solution with isotopes ([6]Li, [45]Sc, [115]In, and [208]Bi) that are not normally encountered in geologic samples. These isotopes are commonly used as the internal standards in the liquid sample analyses using ICP-MS. Figure 2.4 shows the good stability in the sensitivity of ICP-MS during a run period of 9 hours. The signal response for an element from each laser ablation sampling location is corrected from the liquid [115]In response when the laser sampling was conducted. By doing this, any instrumental drift is corrected. Figure 2.5 presents the elemental signal responses in four NIST standard glasses, with a concentration range of about 0.02 to 500 mg/kg for many elements. Note that the Si and Ca concentration is the same in all of the four standard materials, with the value of 336,551 and 85,763 mg/kg, respectively.   The Y-axis is the signal response for each isotope (total counts divided by the [115]I counts per ppt). In essence, Figure 2.5 shows the dimensionless signal per unit laser pulse for each isotope of interest.
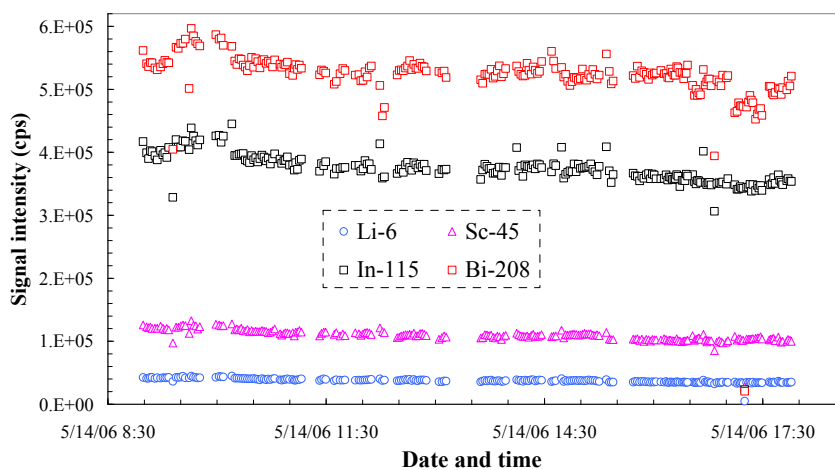
Figure 2.4 Instrumental signal responses for internal standards during laser ablation sampling for LCA-5.

11
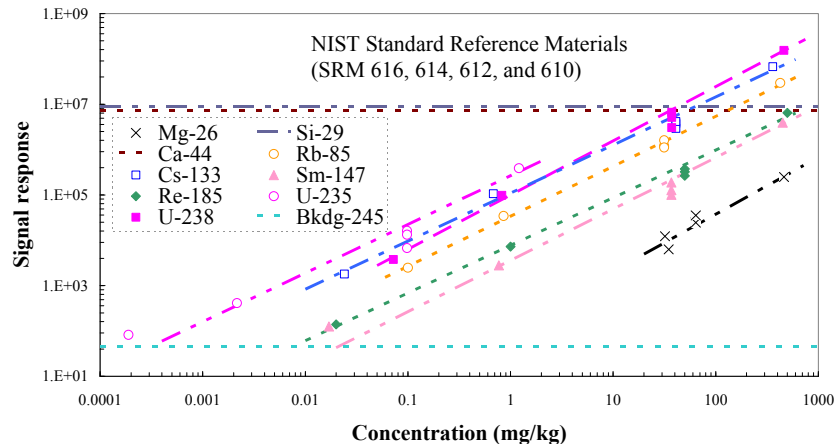
Figure 2.5 Elemental signal responses from NIST Standard Reference Material glasses (SRM 610, 612, 614, and 616).

Quantitative measurement has been one of the major challenges in LA/ICP-MS analyses because of a lack of matrix matching calibration. However, the concentration of an analysis can be calculated from a normalized ratio of both unknown and reference samples (Ghazi et al., 2000; Russo et al., 2002). The method of a single element internal standard calibration strategy is effective for overcoming the potential quantification problems of the LA/ICP-MS. One of the major element constituents of the sample and reference matrix is chosen (such as [44]Ca for dolomite samples) as the reference element. The normalized ratio of analyte to internal standard from the LA/ICP-MS analysis of both the sample and reference standard is then used to calculate the analyte concentration. The calibration curves are obtained from four NIST glasses. Figure 2.6 shows example calibration curves for several isotopes of interest in this study. It is evident that the calibration curves are linear down to 0.01 mg/kg levels for middle-range masses and <0.001 mg/kg for higher masses wherein interferences are less. During depth profiling, normalization accounts for the reduced signal as a function of depth and distinguishes it from a true decrease in the relative element concentration. Normalization during surface profiling also helps to improve data accuracy by considering potential laser performance, e.g., less tracer signal is associated with less [44]Ca signal. In summary, data quality is improved from using the liquid internal standard to correct the ICP-MS drift, and from normalizing methodology to correct laser ablation processes. We assume that the two LCA samples used in the present colloidal transport studies are predominantly comprised of dolomite ($CaMg(CO_3)_2$). We use [44]Ca as the internal standard.
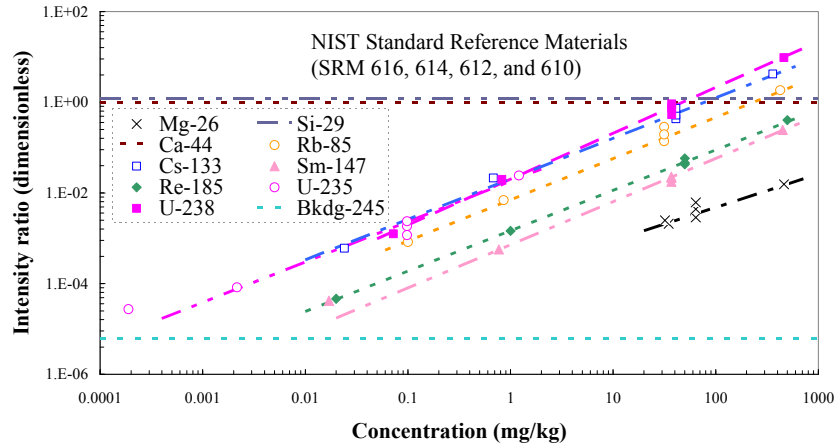
Figure 2.6 Calibration curves using NIST Standard Reference Material glasses (SRM 610, 612, 614, and 616). Y-axis is the dimensionless response (such as these in Y-axis of Figure 2.3) of each isotope divided by that of ^{44}Ca.

2.8 Modeling Approach

Modeling fracture transport was simulated in 2 dimensions using the CRUNCH code (Steefel and Yabusaki, 1995). The modeling strategy is discussed in detail in (Zavarin et al., 2005) and will not be repeated here. Sorption to matrix minerals (calcite/dolomite) and aqueous speciation was accomplished directly in the CRUNCH code based on surface complexation, ion exchange, and aqueous speciation thermodynamic parameters and mineral characteristics reported in (Zavarin and Bruton, 2004a; Zavarin and Bruton, 2004b; Zavarin et al., 2004). Sorption to colloids was implemented using colloid characteristics combined with surface complexation reactions. In essence, colloids were simulated as mobile mineral surfaces with no colloid filtration. Given the simple geometry, short length of our cores, and relatively wide and smooth synthetic apertures, colloid filtration was assumed to be negligible. Diffusion of colloids and colloid-bound radionuclides into the matrix was not allowed. Simulations were run with 2 nodes in the fracture and 12 nodes in the matrix; the core length was divided into 20 nodes for a total of 280 nodes. Matrix diffusion coefficients were based on recent experimental efforts of Reimus et al., (2002) for tuffs and Hershey et al., (2003) for carbonate rock, as will be described in the following section.

3 RESULTS AND DISCUSSION

The two synthetic parallel-plate fracture experiments were conducted. Both used carbonate core sampled from the Nevada National Security Site (ER-6-1). Both cores had similar diameters, lengths, and mineralogy (see Tables 2.1 and 2.2). Both cores used a similar background and sorption solution composition. However, there were two key differences between the two experiments. First, LCA-5 had a fracture aperture of 500 μm which was ten times wider than the aperture of LCA-6. Second, heulandite colloids were used in LCA-5 whereas silica colloids were used in LCA-6.

3.1 Elution Curves

Table 3.1 lists the fraction of each radionuclide that eluted from the column over the timeframe of the flowthrough experiment. The elution of ^{238}Pu and ^{242}Pu is not identical due to their difference in initial oxidation state. For both experiments, the non-sorbing elements eluted quantitatively. In LCA-5, the amount of ^{3}H and ReO$_4^-$ eluted was greater than the calculated amount that was injected into the column. The error is the result of a combination of sample evaporation and uncertainty in the initial concentration for these elements. Given that the major element concentrations did not indicate drastic evapoconcentration of samples, the error lies primarily with the uncertainty in initial concentration. However, some sample evaporation was observed as well. In LCA-6, the autosampler device was encased in a humidified chamber to reduce the potential for sample evaporation. This change, combined with stricter control of flow rates and sorption solution composition resulted in much better quantitation.

Table 3.1 Fraction of radionuclides eluted over the timeframe of each experiment.

	^{3}H	Re	U	^{238}Pu (LSC)	^{242}Pu (ICP)	Sm
LCA-5	1.40[a]	1.60[a]	0.87	0.50	0.44	0.19
LCA-6	0.96	1.08	1.01	0.47	0.72	0.23

[a] Value >1 is an artifact of sample evaporation during the experiment and uncertainty in the initial concentration of these radionuclides. Evaporation problem was corrected in experiment LCA-6 by enclosing auto-sampler in humidified chamber.

3.1.1 LCA-5

Elution of all radionuclides is presented in Figures 3.1 and 3.2. Based on ^{3}H and Re breakthrough profiles, diffusion into the carbonate matrix is very slow. However, the long tailing of both these species is indicative of a combination of matrix diffusion and dispersion. The very close match in the tailing of these two non-sorbing tracers suggests that dispersion is the dominant component controlling the tailing behavior observed in LCA-5.

Sm, U, and Pu are all retarded, though their breakthrough is observed. Sm breakthrough is predominantly in the form of an attenuated pulse breakthrough coincident with the non-sorbing tracer breakthrough. We attribute this transport behavior to that of colloid-facilitated transport. In the absence of colloids (Zavarin et al., 2005), no Sm was observed in the effluent. The affinity of Sm for calcite is very high (Zavarin et al., 2005) and its transport is expected to be drastically retarded in the absence of colloids. Importantly, less than 20% of Sm was recovered from the column effluent. The loss of Sm from the eluent can be attributed to a combination of desorption of Sm from colloids and sorption to the carbonate matrix and colloid filtration. The size of the synthetic aperture and its geometry was expected to minimize the role of filtration in these experiments. However, as will be shown later, deposition of colloids on the fracture surfaces was unavoidable.

Nearly all the U introduced into the column was recovered in the effluent. Based on the observed transport behavior and its very weak affinity for aluminosilicate minerals, colloids did not play a role in U transport. Though U(VI) sorption to calcite is quite weak (Zavarin and

Bruton, 2004a), trace quantities of iron oxides and/or silicates (1.6% quartz detected by XRD) may have contributed to U retardation.

Pu breakthrough has been plotted for both [238]Pu and [242]Pu. The [238]Pu was measured by LSC and the stock solution was composed of 95:5 Pu(V/VI):(IV). The [242]Pu was measured by ICP-MS and the stock solution was composed of 40:60 Pu(V/VI):(IV). The difference in their breakthrough can be attributed to the difference in initial oxidation state. For example the small peak in [242]Pu that coincides with Sm(III) breakthrough can be attributed to colloid-facilitated Pu(IV) transport. As Pu(V) is a relatively weak sorber on aluminosilicates, colloid-facilitated transport of Pu(V) is unlikely. Instead, the broad breakthrough peak observed for [238]Pu can be attributed to retardation of aqueous Pu(V) on the rock matrix. Importantly, it should not be assumed that the Pu oxidation states in these experiments are invariant with time. In fact, we expect Pu(V) to reduce and sorb to both the calcite matrix and the aluminosilicate colloids with time (Zavarin et al., 2005). At field spatial and temporal scales, sorbed Pu will be predominantly in the +4 state while the aqueous phase may be in the +5 state (Powell et al., 2006). Nevertheless, the results from LCA-5 suggest that Pu transport will be governed by a combination of colloid-facilitated and aqueous transport mechanisms that will evolve with time and depend on the oxidation-state of Pu.
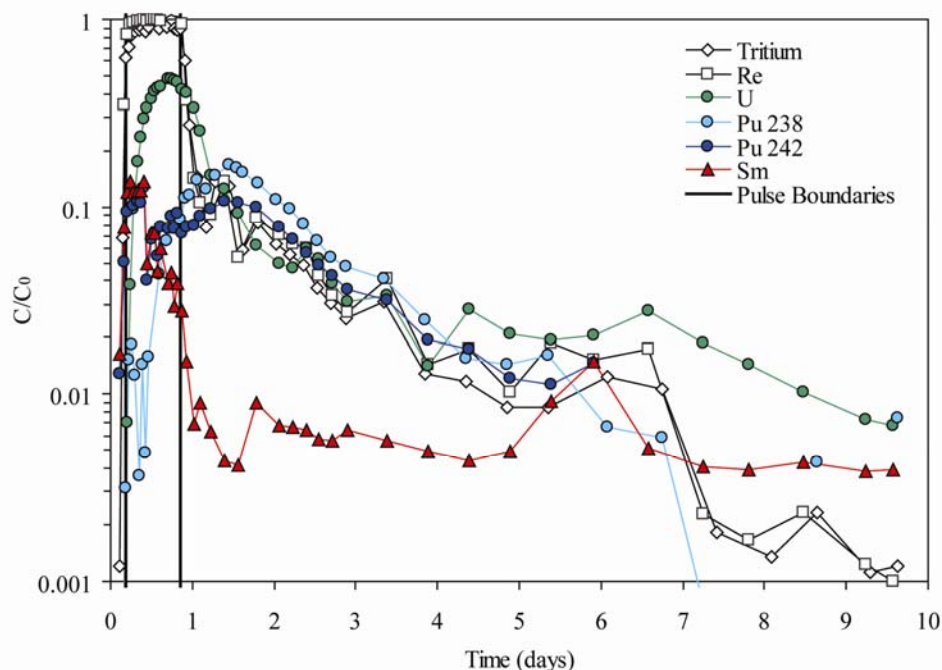
Figure 3.1 LCA-5 breakthrough plot (log scale y-axis). The two vertical lines represent the beginning and end of the sorption pulse.
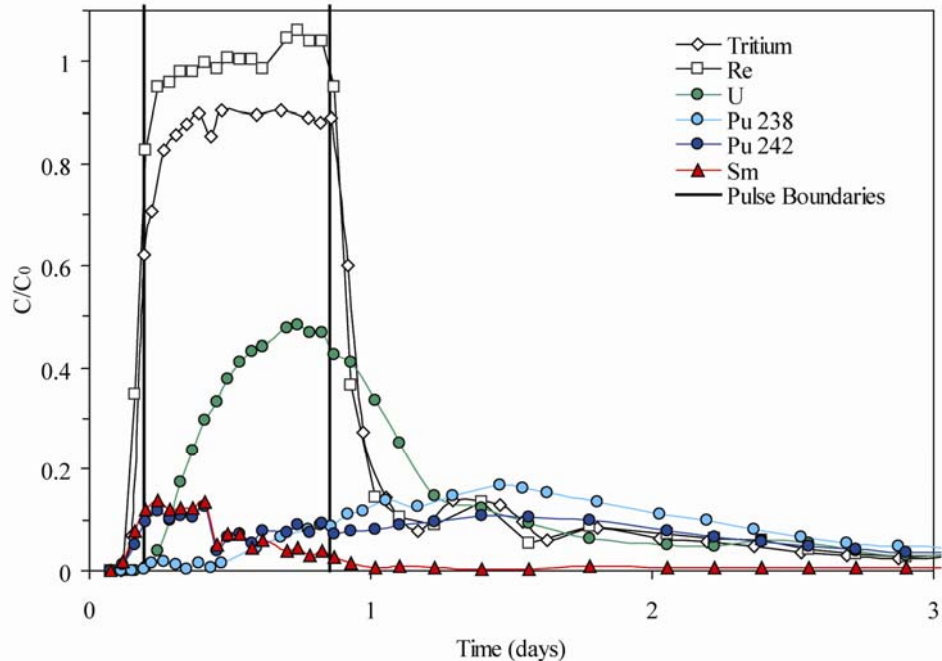
Figure 3.2 LCA-5 breakthrough plot (linear scale y-axis). Sorption pulse timeframe magnified. The two vertical lines represent the beginning and end of the sorption pulse.

3.1.2 LCA-6

Elution of all radionuclides is presented in Figures 3.3 and 3.4. Matrix diffusion of ^{3}H and Re is more pronounced than LCA-5 due to the small aperture of the LCA-6 fracture (0.050 mm). The long tailing of both these species is indicative of a combination of diffusion-controlled retardation and dispersion. The divergent breakthrough of Re and 3HHO in the tailing is indicative of matrix diffusion, which appears to be slow at the scale of these experimental conditions.

Sm, U, and Pu are all less retarded than in LCA-5. This is, in part, due to the shorter residence time of these radionuclides in the fracture. Sm breakthrough is predominantly in the form of an attenuated pulse coincident with the non-sorbing tracer. However, some tailing exists as well. The unretarded breakthrough of Sm is indicative of colloid-facilitated transport. However, as in LCA-5, only a fraction of Sm was recovered from the column effluent. Thus, a substantial fraction of the Sm is lost to the carbonate core along the flow path.

All the U introduced into the column was recovered in the effluent and very little retardation was observed. U breakthrough followed the profile on the non-sorbing tracers. There are no mineralogic or geochemical parameter that can explain the lower sorption in this experiment compared to LCA-5.

Pu breakthrough has been plotted for both ^{238}Pu and ^{242}Pu. The ^{238}Pu breakthrough (95:5 Pu(V/VI):(IV)) is somewhat more attenuated than ^{242}Pu (40:60 Pu(V/VI):(IV)). In this core, Pu(V) sorption is quite weak and much of the breakthrough is coincident with the non-sorbing tracers. Transport of Pu(V) is expected to be predominantly as an aqueous phase. The ^{242}Pu breakthrough can be attributed to a combination of aqueous Pu(V) transport and colloid-

16

facilitated Pu(IV) transport. Colloid-facilitated Sm(III) transport coincides with the increased breakthrough of ^{242}Pu versus ^{238}Pu. As in LCA-5, it should not be assumed that the Pu oxidation states in these experiments are invariant with time. However, ^{242}Pu will certainly be more reduced that ^{238}Pu.
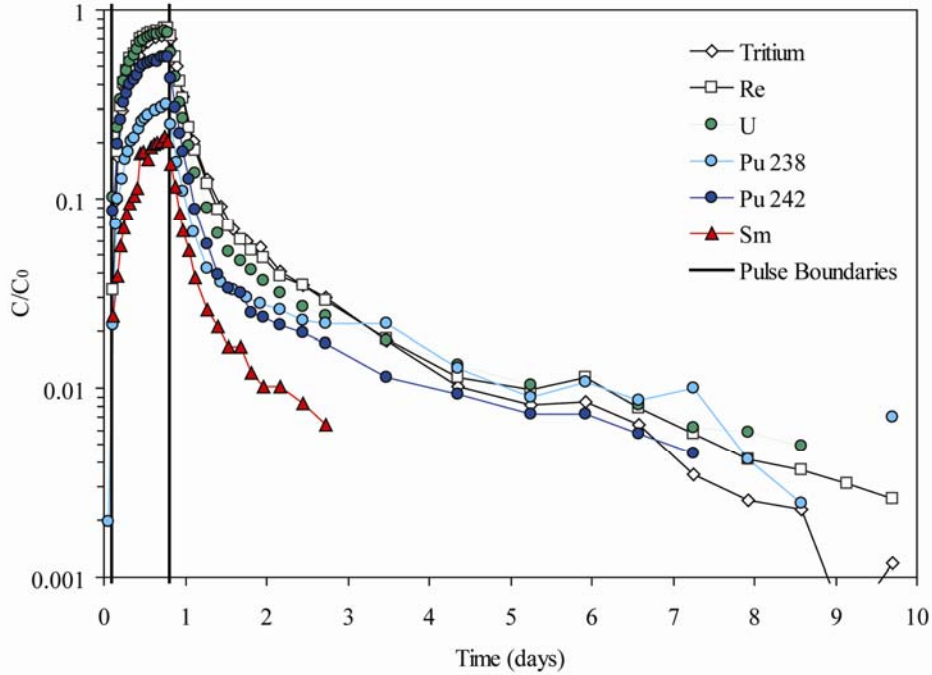
Figure 3.3 LCA-6 breakthrough plot (log scale y-axis). The two vertical lines represent the beginning and end of the sorption pulse.
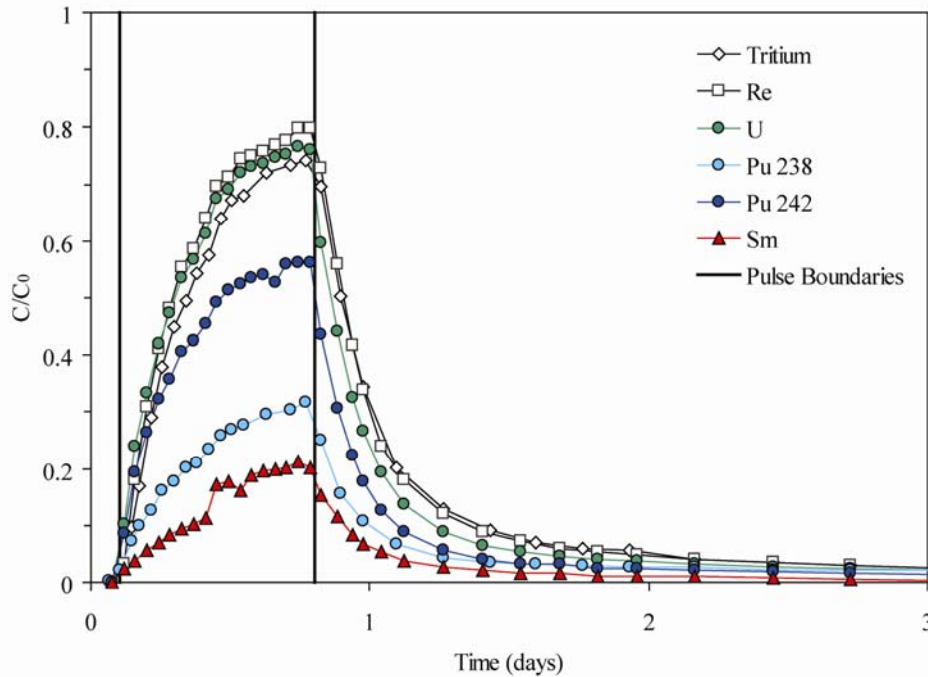
Figure 3.4 LCA-6 breakthrough plot (linear scale y-axis). Sorption pulse timeframe magnified. The two vertical lines represent the beginning and end of the sorption pulse.

3.2   Autoradiography

3.2.1   LCA-5

Autoradiography was performed on both cores. The exposure times varied for each of the cores and are shown in Table 3.2. The LCA-5 core did not contain as many occlusions and rough surfaces as the LCA-6 core and there were no visible iron oxide regions. One of the plates used for alpha radiography of LCA-5 was slightly warped and created a thin air layer (capable of attenuating alpha particles) between the core surface and the plate. The location of the air layer corresponds to the region of low alpha activity shown in the center of the core in Figure 3.5. Therefore, the extent of alpha activity in this region cannot be accurately determined. In regions where there was minimal separation between the plate and the core surface, alpha activity was widely distributed throughout the core. There are regions of higher activity near the edges of the fracture that may indicate preferential flow-paths. However, activity observed at both the inlet and outlet ports demonstrates that alpha emitting radionuclides ([238]Pu) reached the outlet port of the column. This is consistent with the observed [238]Pu in the effluent.

Table 3.2 Exposure times for α-radiography on the rock cores.

Core	Exposure Time (days)
LCA-5	6.75
LCA-6	5.75

18

Under microscopic observation, the fracture surface was coated with intertwined, needle-like white solids. The morphology of the white solids is significantly different than the surrounding core. Small amounts of this material were collected and placed in acid; little or no strong effervescence was observed. Thus, it is likely that a significant fraction of this material is colloidal heulandite. A high concentration of this material was observed near the core outlet (inset Figure 3.5) near an exposed cavity along with a relatively high concentration of alpha activity. Based upon their observed co-association, the material appears to significantly control the distribution of alpha emitting radionuclides within the core. Furthermore, they suggest that colloid filtration may have attenuated the breakthrough of alpha-emitting radionuclides (e.g. ^{238}Pu).

In addition to the white solids, several yellow and blue fibers were observed which appear to be synthetic. A large grouping of these fibers associated with the white material was observed in LCA-6. Intertwinement of the fibers with the white material indicates that the fibers were introduced before or during the experiment and are not an artifact of post-experiment sample processing. The identity of the fibers has not been ascertained. With the exception of one area, the fibers and white material appeared to be widely dispersed over the LCA-5 core surface. The synthetic fibers within LCA-5 did not appear to be correlated with alpha activity.
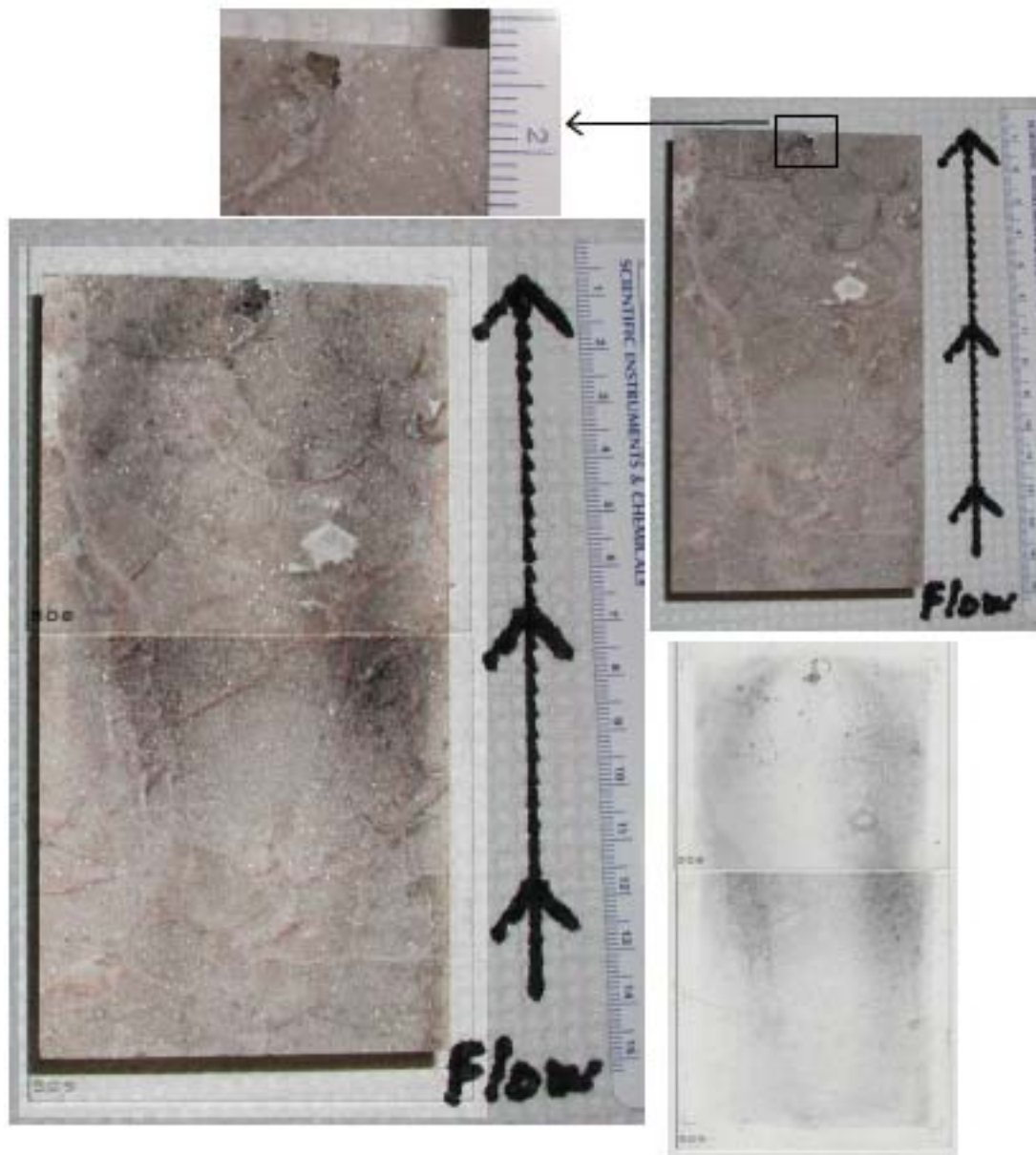
Figure 3.5 One-half of LCA-5 core (top right) and developed radiography plates (bottom right). Image of developed film is overlain on the core (left) and the arrow is noting direction of flow during the flowthrough experiment. Dark spots on the radiography plates indicate regions of concentrated alpha activity. Expanded inset of LCA-5 core outlet is shown in top left position.

3.2.2 LCA-6

Alpha tracks were observed throughout the core indicating a wide distribution of alpha activity. The appearance of α-tracks at the outlet is consistent with the observation of alpha emitting radionuclides in the effluent during the flowthrough experiment. However, the density of α - tracks at the outlet of the core was visibly lower than several other regions.

There are three noteworthy regions of concentrated alpha activity on the core (Figure 3.6). Section A shows a strong correlation between a small fracture running along the left side of the core and concentrated alpha activity. The fracture is relatively thin and shallow, allowing the short-range alpha particles to reach the radiography plate. Section B corresponds to another small fracture that appeared to sequester ^{238}Pu. The alpha tracks in region B are darker, relative to the other alpha tracks, indicating more concentrated alpha activity. Similar to LCA-5, low-power microscopic observations revealed the presence of both white material and synthetic fibers. The "Y" shaped feature of alpha activity within region B exactly corresponds to the distribution of the white material within that region, but are only observable under magnification. When small amounts of the white material were collected and placed in acid; little or no strong effervescence was observed. It suggests that a significant fraction of this material is colloidal silica. Therefore, similar to the observation made for LCA-5, there is a correlation between the presence of the white material and alpha activity and it is suggestive of colloid filtration.

The yellow and blue synthetic fibers observed on LCA-5 were also observed under low-power magnification of LCA-6. A large grouping of the fibers associated with the white secondary precipitates and/or colloids is shown in Figure 3.7. Several fibers were observed throughout the core, but the image in Figure 3.7 shows the highest concentration of fibers observed at one point. As with LCA-5, intertwinement of the fibers with the white material indicates that the fibers were introduced before or during the experiment. Furthermore, the association of alpha-activity with the white material in both cores, and the lack of association with the synthetic fibers, indicates that the white material controls the distribution of alpha emitting radionuclides on both core surfaces, while the synthetic fibers have little or no influence.

Region C (Figure 3.6) contains some red solid phases which are presumably iron oxides or iron oxide coatings on the host matrix. This region has a high concentration of alpha activity. An expanded image of the core surface in region C (Figure 3.8) shows the region is not flat. The interstitial space between the core surface and the radiography film may attenuate alpha particles. Therefore, if additional activity was present within the occlusion, it would not have been detected using the alpha radioactivity technique employed in these experiments. No alpha activity was observed associated with the reddish mineral phases in the lower right corner of the core. This may be due to preferential flow in the center of the fracture resulting from the pinhole opening at the core inlet.
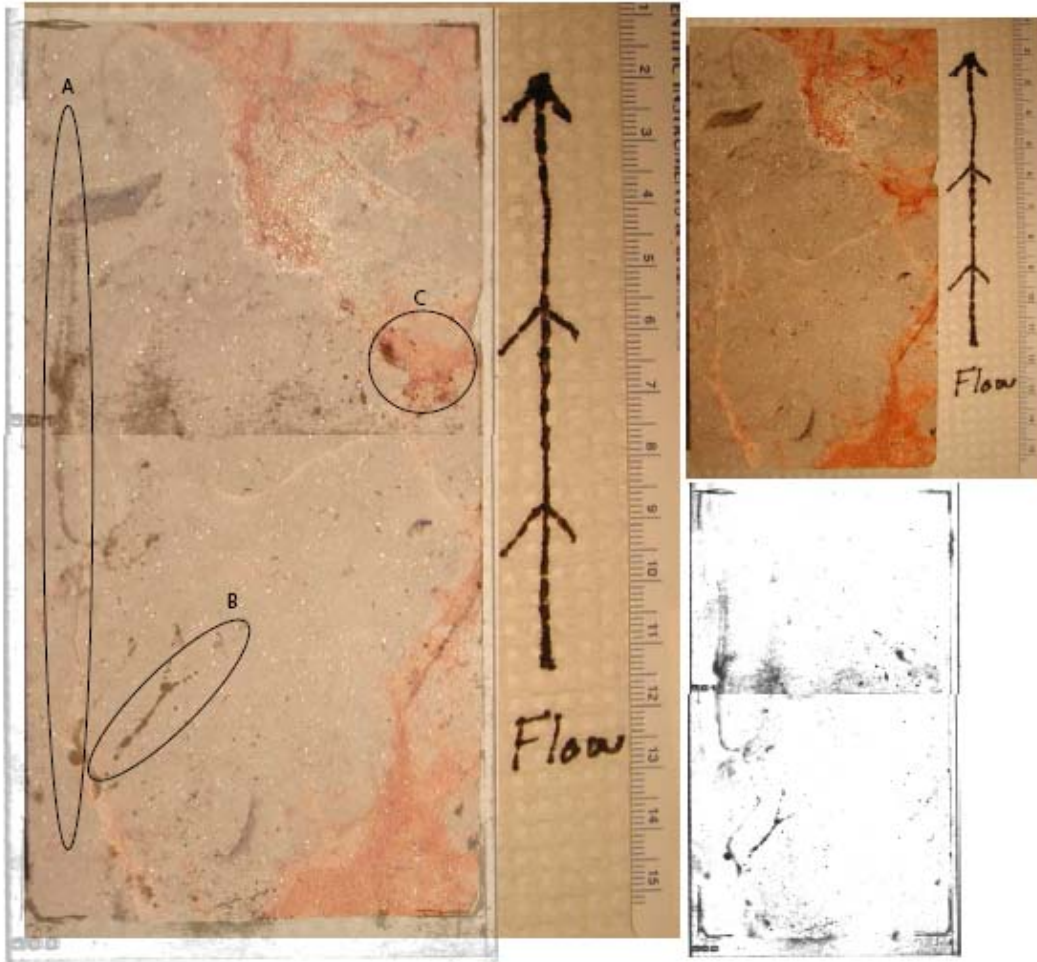
Figure 3.6 One-half of LCA-6 core (top right) and developed radiography plates (bottom right). Image of developed film is overlain on the core (left) and the arrow is noting direction of flow during the flowthrough experiment. Dark spots on the radiography plates indicate regions of concentrated alpha activity. Areas noted A, B, and C (left) show areas of interest as discussed in the text.

Digital Images of Core LCA-6 from
Flow-through colloid transport experiment

Note: Inset squares in approximate position
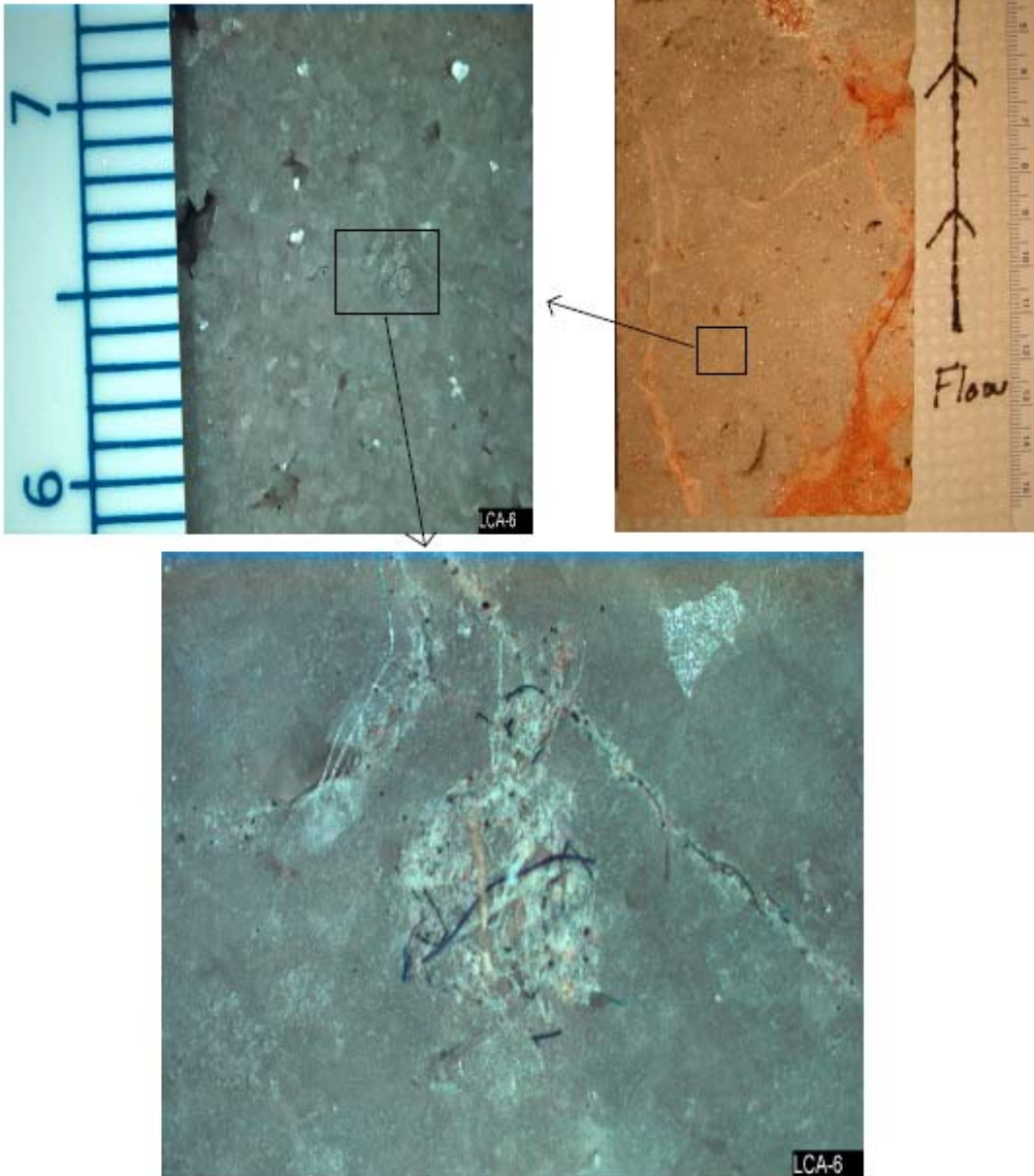
Figure 3.7 Digital image of precipitates/colloids and synthetic fibers observed in region B of Figure 3.6.
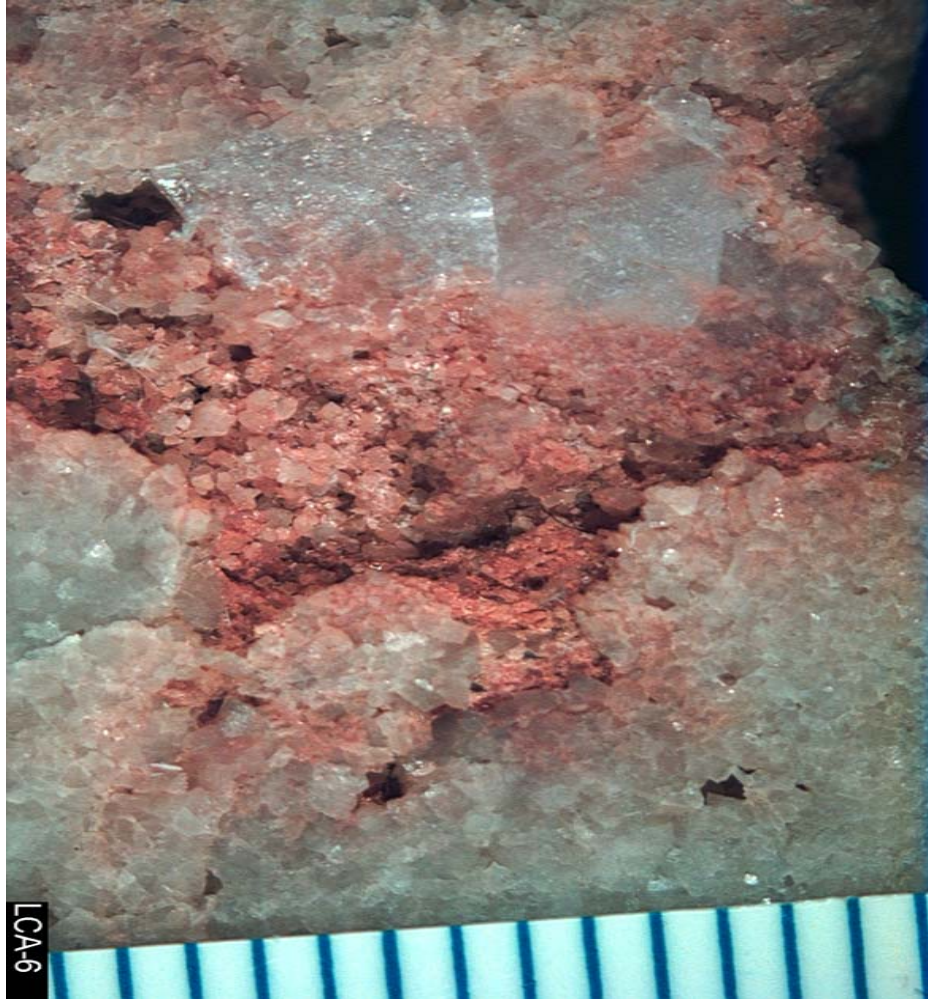
Figure 3.8 Digital image of region C from Figure 3.6. Scale markings represent 1mm.

3.3   Laser Ablation

For LCA-5, Re breakthrough data are indicative of non-sorbing transport. Consistently, LA/ICPMS data show uniform [185]Re distribution across the fracture surface at near background levels (Figure 3.9a). A similar distribution pattern was observed for [238]U, consistent with its nearly quantitative elution from the fractured core. Some higher concentrations in the latter half of the fracture surface reflect residual U(VI). Breakthrough data indicate that only a fraction of the [147]Sm and [242]Pu are eluted. However, both [147]Sm and [242]Pu are also uniformly distributed in LCA-5. The absence of a "migration front" is likely due to a combination of transport processes controlling migration of these radionuclides (i.e. colloid-facilitated transport, colloid filtration, matrix diffusion, and matrix sorption.
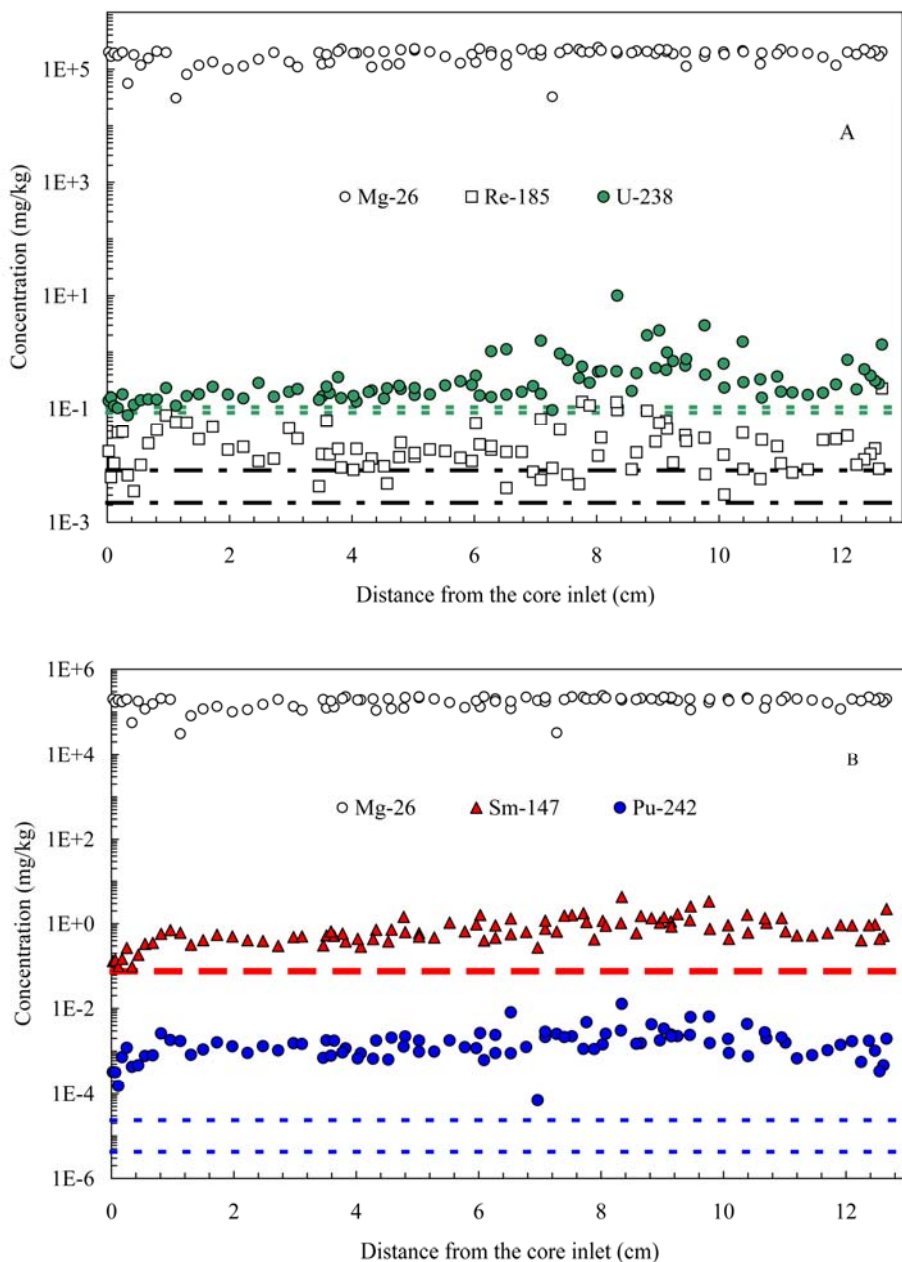
Figure 3.9 Distribution of isotopes obtained from surface profiling in LCA-5 core using LA/ICP-MS. Symbols represent data; lines represent background intensity ratios (average ± standard deviation). The distribution of intrinsic Mg-26 is also shown.

Results from depth profiling confirm that transverse migration had occurred for the applied tracers. Figure 3.10 shows the profiling results obtained at two locations ~2.5 mm from the core inlet and perpendicular to the fracture surface. Compared to the uniform distribution pattern of [26]Mg, all the added tracer elements exhibit a higher surface concentration than the locations deep in the rock matrix. This is particularly evident for [242]Pu, which has a low background level. Concentrations of [242]Pu decrease gradually and approach background at 50-100 μm.

The LA/ICPMS results from LCA-6 generally reflect the same transport behavior observed in LCA-5. The non-sorbing ^{185}Re was mostly flushed out and little remains on the fracture surface (Figure 3.11). Some ^{238}U appears to have accumulated near the core inlet. However, the concentration is only slightly above background and may be related to the trace iron oxide located near the core inlet. Similar accumulation near the core inlet is observed for ^{147}Sm and ^{242}Pu. ^{242}Pu is also observed over the entire length of the core, consistent with the LCA-5 data.

Interestingly, measurement of Fe and ^{242}Pu simultaneously over a number of locations on the LCA-5 fracture surface confirms the preferential sorption of Pu to iron oxides vs. calcite (Figure 3.12). This was also observed when autoradiography was combined with optical microscopy. Nevertheless, due to the very small quantities of iron oxide in these samples, calcite will likely be the dominant sorber in the carbonate rock matrix.
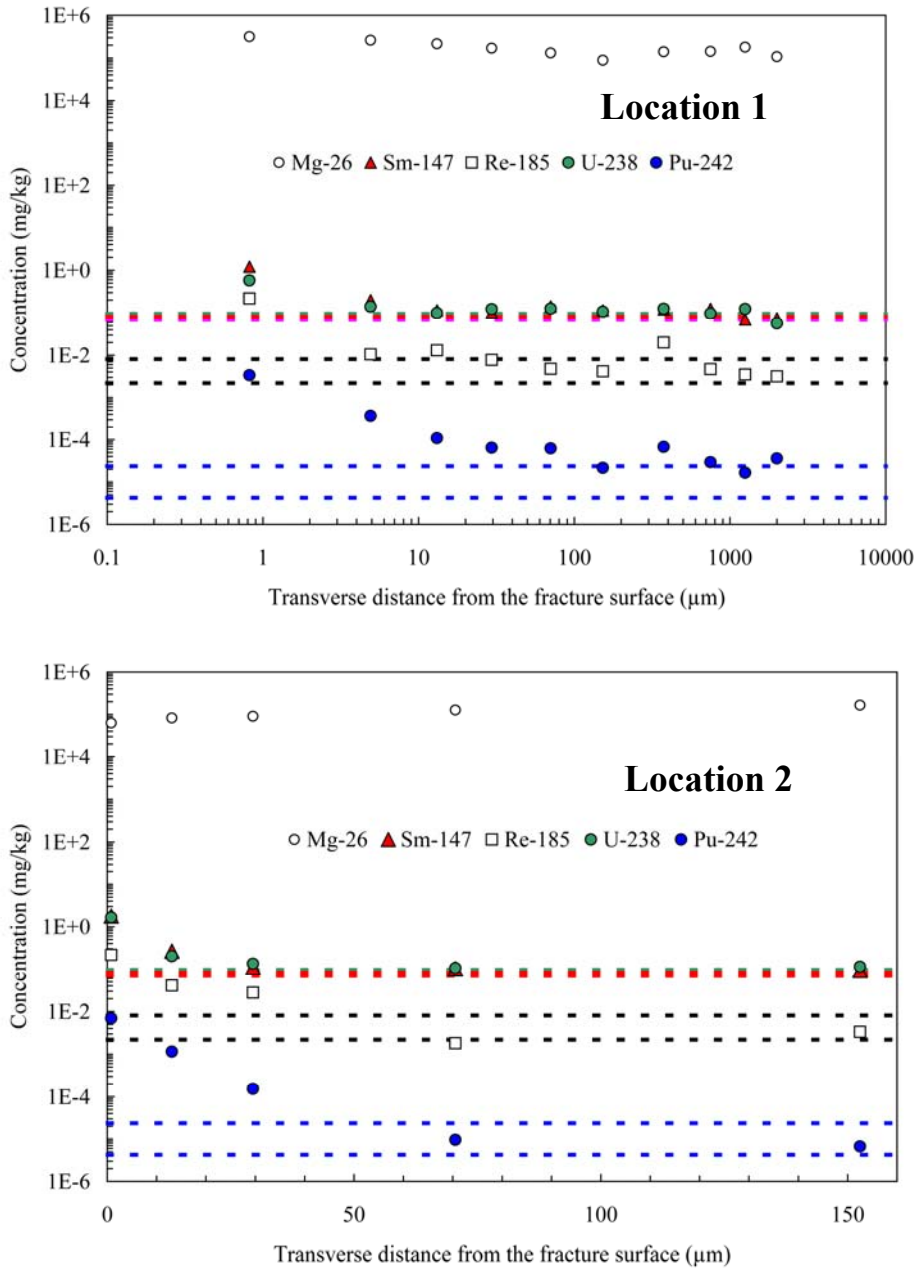
Figure 3.10 Distribution of several isotopes obtained from depth profiling in LCA-5 core sample using LA/ICP-MS at two locations near the core inlet. Symbols represent data; lines represent background intensity ratios (average ± standard deviation).
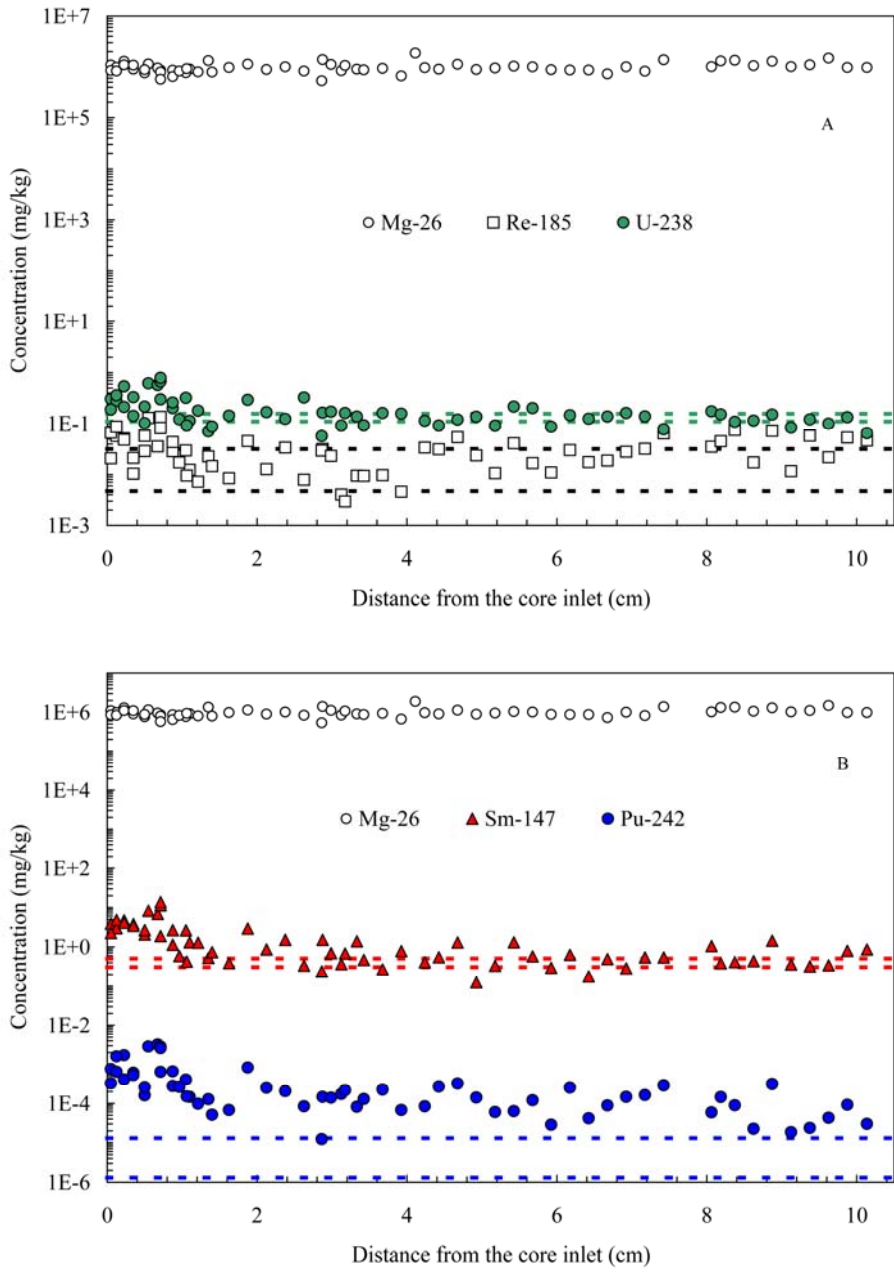
Figure 3.11 Distribution of isotopes obtained from surface profiling in LCA-6 core using LA/ICP-MS. Symbols represent data; lines represent background intensity ratios (average ± standard deviation).

Sample spot (laser pulse)	Fe conc. (g/kg)	[242]Pu conc. (ng/kg)
1 (20)	13.7	750
2 (20)	10.2	641
3 (20)	59.4	1704
4 (20)	20.8	604
5 (20)	1.89	161
6 (5)	131.2	2871
7 (5)	4.04	638
8 (20)	3.57	238
9 (20)	0.539	146
10 (20)	0.885	127
	Correlation: 0.979	
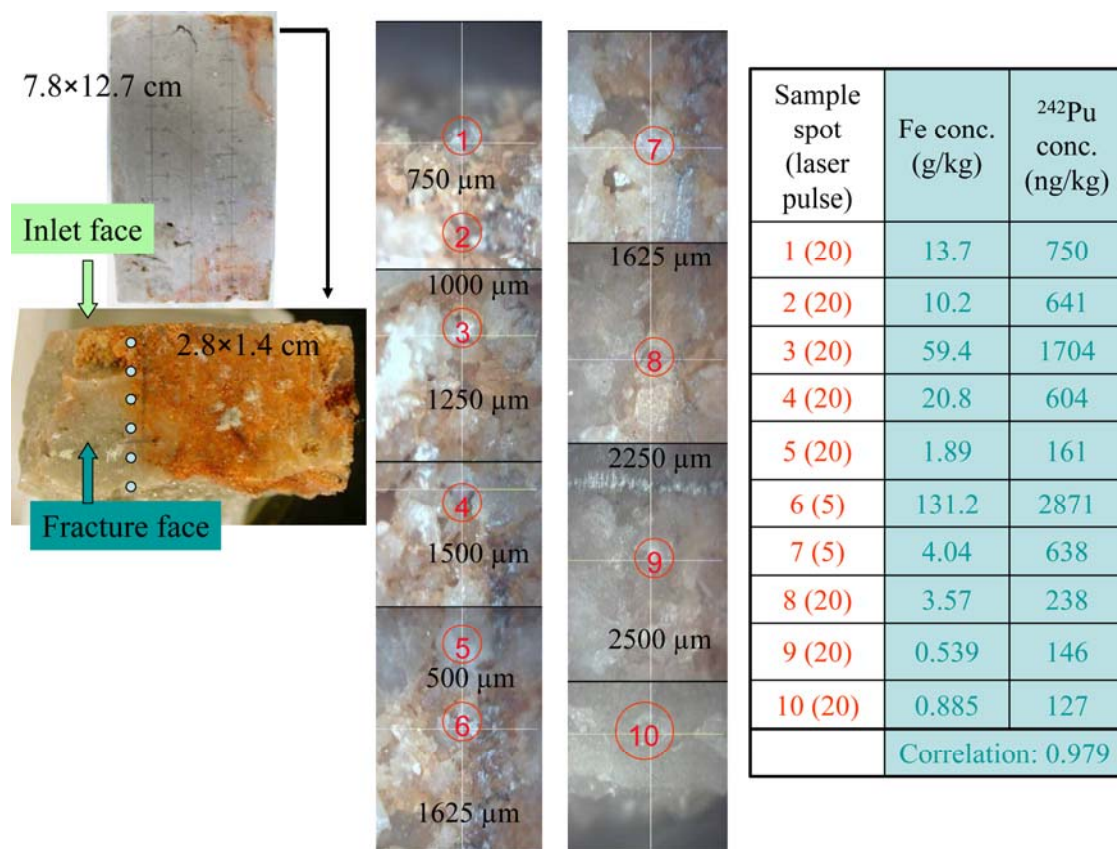
Figure 3.12 Distribution of Fe and Pu on LCA-6 fracture surface using LA/ICP-MS. Strong correlation is indicative of the preferential sorption of Pu to iron oxide vs. calcite.

4   REACTIVE TRANSPORT MODELING

Experiments LCA-5 and LCA-6 were modeled using the CRUNCH code (Steefel and Yabusaki, 1995). CRUNCH can simulate multi-component mass transport in porous/fractured media under non-isothermal conditions, including consideration of zonal variations in mineralogy and fluid chemistry. Aqueous speciation, surface complexation, ion exchange, mineral dissolution/precipitation, and radionuclide decay are all modeled explicitly. Details regarding the CRUNCH code and its use are reported in (Zavarin et al., 2005) and will not be repeated here.

A large number of parameters and data are needed to simulate reactive transport with the CRUNCH code. The water chemistry used in the model was based on the average composition of the effluent (see Appendix). Radionuclide concentrations were taken from Table 2.4. The rock mineralogy was assumed to be pure carbonate. The core characteristics (porosity, core dimensions, aperture) and flow rate (0.02 mL/min) were taken from Table 2.1. The time of the tracer injection pulse was taken from Table 2.5. Aqueous complexation and surface complexation reaction constants and mineral surface area/reactive site density were taken from (Zavarin and Bruton, 2004a; Zavarin and Bruton, 2004b) and (Zavarin et al., 2002). The concentration of colloid >SiOH and >AlOH reactive sites was calculated based on the colloid

mineralogy, load, particle size, and a nominal reactive site density of 2.31 sites/nm^2. However, the surface complexation reaction constants and calcite surface area were adjusted in the model to achieve the best fit to the data. Because all model parameters were held constant during modeling, data fitting parameters could be reduced to parameters describing three processes: (1) sorption to colloids, (2) matrix diffusion, and (3) matrix sorption. Breakthrough of all radionuclides in a single experiment was modeled simultaneously. Matrix diffusion was calibrated to the breakthrough of the non-sorbing tracers. Diffusion coefficients in water for all radionuclides were taken from the literature (25°C). ^{3}H and Re diffusion in water was 2.2×10^{-9}, 1.5×10^{-9}, respectively (Kemper, 1986; Mills, 1973; Lide, 2000; Reimus et al., 2002; Hershey et al., 2003). The diffusion of all other radionuclides (U, Pu, and Sm) was assumed to be equivalent to the diffusion of Tc in water (1.5×10^{-9} m^2/s from (Reimus et al., 2002)); it was impractical to try to accurately predict the diffusivity of these radionuclides since multiple aqueous species were predicted to be present in solution and each would diffuse at a different rate. The tortuosity parameter was used to fit the apparent radionuclide diffusion. Dispersivity was set to 0 in our model. When run in the global implicit approach, the CRUNCH code can suffer from significant numerical dispersion. As described in (Zavarin et al., 2005), model results were not sensitive to dispersivity because its effect was masked by numerical dispersion. In any case, dispersion is expected to be low since the fracture geometry is smooth and regular.

Table 4.1 and Figures 4.1 to 4.7 summarize modeling results. Table 4.1 lists the transport parameters varied to fit the breakthrough data (tortuosity (τ), matrix retardation factor, fraction sorbed to colloids). All other parameters used in the modeling were either measured directly or based on values from the literature (e.g. D_0).

Table 4.1 Predicted and fitted radionuclide retardation and diffusion parameters for carbonate cores.

	^{3}H	Re	U	Pu(IV)	Pu(V)	Sm
			LCA-5			
τ[a]	1	1	1	1	1	1
Rmatrix	1	1	$10^{1.7}$	$10^{7.0}$	$10^{2.5}$	$10^{6.9}$
Percent on colloids	0	0	0	98	0	97
			LCA-6			
τ	1	1	1	1	1	1
Rmatrix	1	1	$10^{0.1}$	$10^{3.2}$	$10^{1.1}$	$10^{7.7}$
Percent on colloids	0	0	0	98	0	99.5

[a] To achieve a good fit, the porosity of the rock was increased from 1% to 2%.

The tortuosity, free water diffusivity (D_0) and porosity parameters are all highly correlated. As a result, only one of the three parameters can be fitted during modeling. The D_0 and porosity for each radionuclide and core were taken from the literature and measured directly, respectively. However, based on the fact that the fitted tortuosity was consistently 1.0, we suspect that the actual porosity of the carbonate rock may be somewhat higher than the measured value. In fact, to achieve a good fit to the data, the porosity of LCA-5 was increased from the measured value of 1% to a fitted value of 2%.

For both LCA-5 and LCA-6, the breakthrough of non-sorbing ^3H and Re could be modeled quite well using the measured fractured core geometry, rock properties, and fluid flow rates and adjusting only the tortuosity and the porosity of LCA-5 (Figure 4.1). The fit to the LCA-5 data was somewhat hampered by the mass balance issues associated with this experiment. Nevertheless, the model fit the data quite well. Importantly, the modeling results indicate that the carbonate core will be accessible to diffusion and will contribute to the retardation of non-sorbing tracers. The modeled distribution of non-sorbing ^3H and Re in the matrix at the end of the LCA-5 flowthrough experiment is plotted in Figure 4.2.
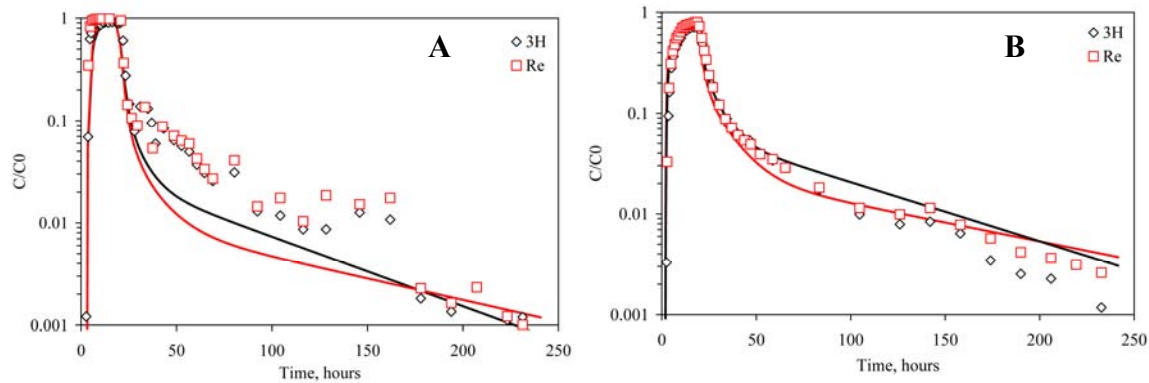
Figure 4.1 Model fits to LCA-5 (A) and LCA-6 (B) non-sorbing tracer elution data.
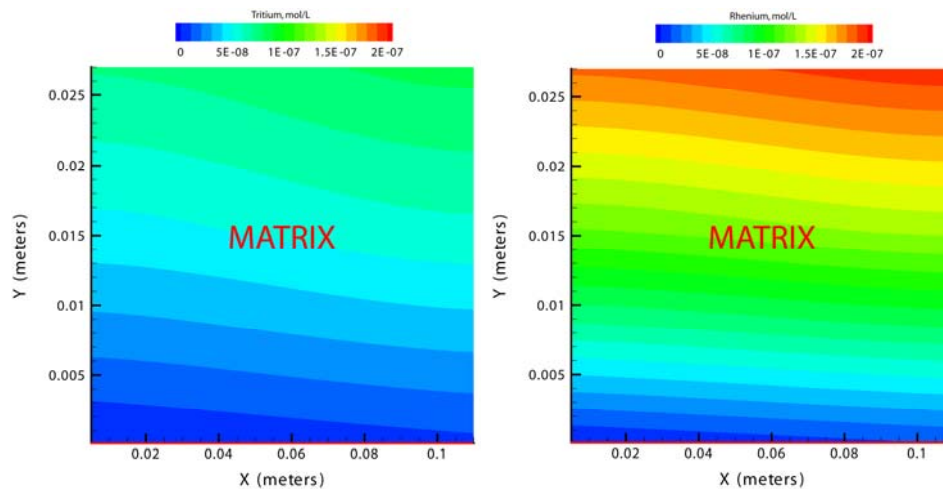
Figure 4.2 LCA-5 model of aqueous tracer radionuclide distribution at end of flowthrough experiment.

Generally, U(VI) sorbs weakly to calcite when in the +6 oxidation state (Zavarin and Bruton, 2004b). This is consistent with the modeled U(VI) retardation values of 50 ($10^{1.7}$) and 1.3 ($10^{0.1}$) for LCA-5 and LCA-6, respectively (Table 4.1). The LCA-5 and LCA-6 fracture breakthrough data could be modeled very well with diffusion and matrix sorption (Figures 4.2). Interestingly, U(VI) sorption in LCA-5 was significantly greater than in LCA-6. The source for the greater retardation is not known but could be address by trace concentrations of iron oxide found in carbonate rock.
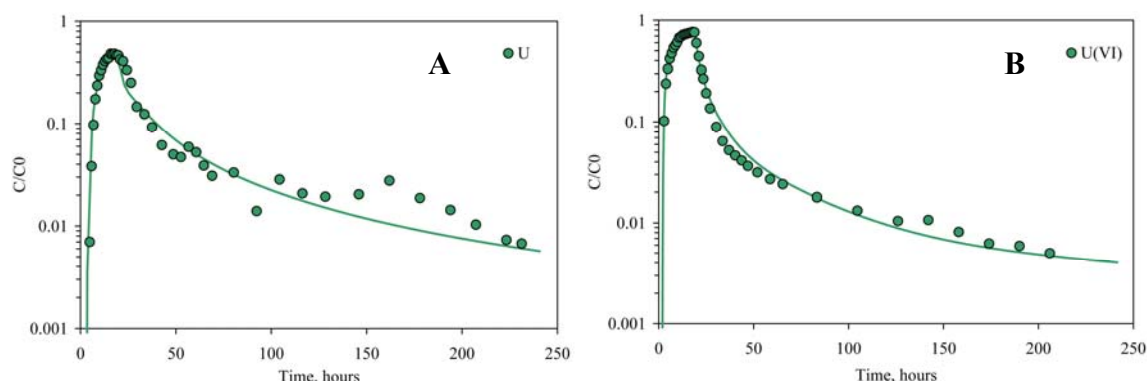
Figure 4.3 Model fits to LCA-5 (A) and LCA-6 (B) U(VI) elution data.

The migration of Sm(III) could not be modeled without accounting for colloid-facilitated transport. Given the very strong affinity of Sm(III) and all trivalent lanthanides and actinides for mineral surfaces, we would expect most of the soluble Sm(III) to be colloid-bound in both fracture transport experiments. To model the data, Sm(III) diffusion into the carbonate matrix was restricted to the non-colloid-bound species. Colloid filtration was not included in this model. A very good fit to the LCA-5 and LCA-6 data could be achieved (Figure 4.4). In both cases, >95% of the aqueous Sm((III) was bound to colloids while the matrix retardation factor was very high ($10^{6.9}$ and $10^{7.7}$). The high retardation resulted in predicted Sm deposition into the first ~50 µm of the matrix (Figures 4.5). The results are in general agreement with the depth profiling results shown in Figure 3.10 for core LCA-5. The distribution of Sm along the length of the fracture is also qualitatively consistent with LA/ICP-MS data reported in Section 3.
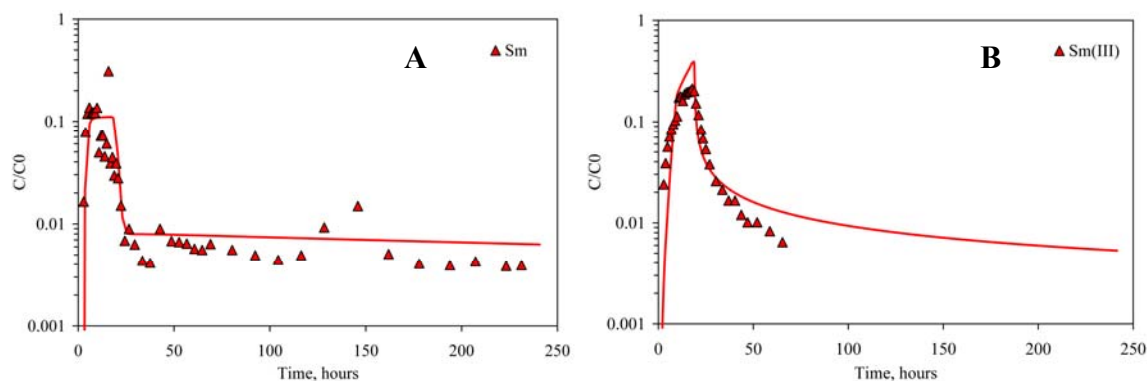
Figure 4.4 Model fits to LCA-5 (A) and LCA-6 (B) Sm(III) elution data.
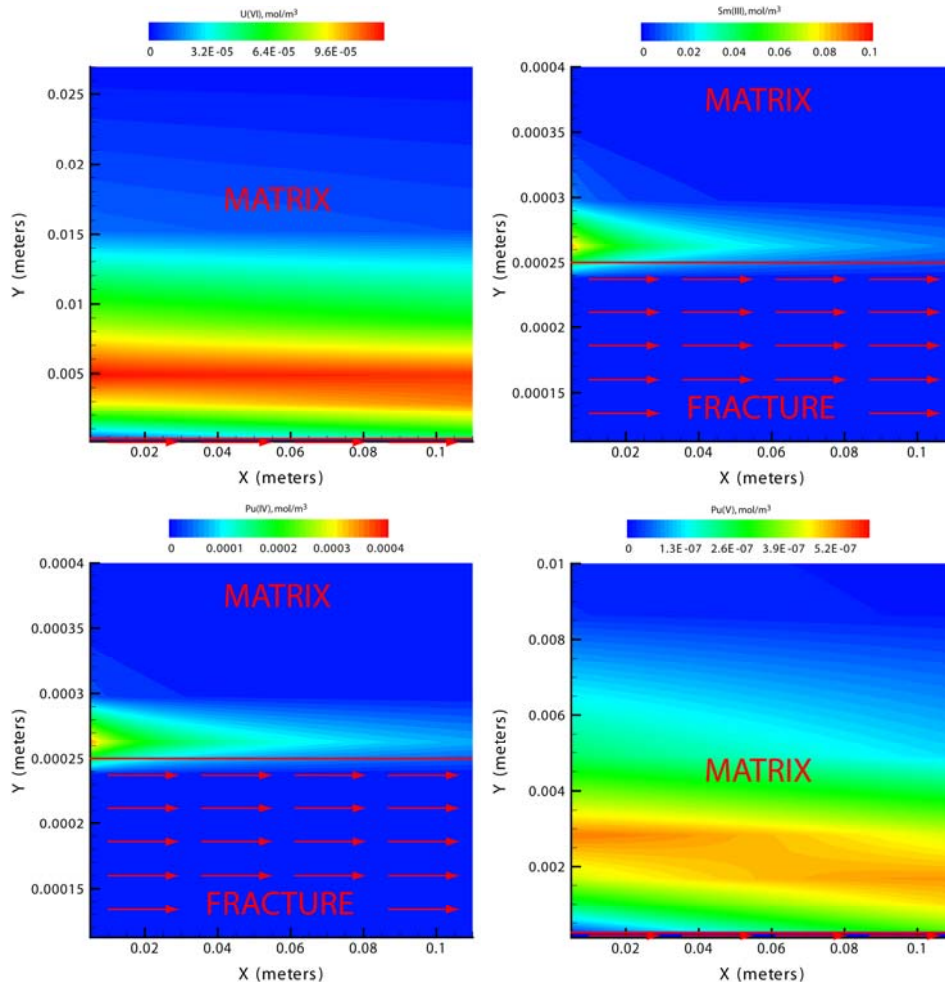
Figure 4.5 LCA-5 model of sorbed radionuclide distribution for U, Sm, Pu(IV), and Pu(V) at end of flowthrough experiment.

Modeling the migration of Pu is complicated by the fact that multiple oxidation states with differing sorption affinities for both the colloidal and matrix minerals exist. To simplify the Pu transport model, we assumed that the oxidation state of Pu was constant and equal to the oxidation state of the stock solutions. Thus, [238]Pu was composed of 95% Pu(V) and 5% Pu(IV); [242]Pu was composed of 60% Pu(IV) and 40% Pu(V). In fact, we expect some of the Pu(V) to be reduced to Pu(IV) as it sorbs to the colloids or matrix. However, the rate of this reduction reaction is not known. A second assumption was that Pu(V) will not sorb to aluminosilicate colloids. This is not altogether unreasonable given the much weaker sorption of Pu(V) compared to Pu(IV) to these minerals (Zavarin and Bruton, 2004a). Thus, Pu transport was modeled by adjusting Pu(IV) sorption to colloids, Pu(IV) sorption to the matrix, and Pu(V) sorption to the matrix.

Given the simplicity of our model, the resulting fits to the breakthrough data are quite good (Figure 4.6). The initial [242]Pu peak in LCA-5 can be attributed to Pu(IV) colloid-facilitated transport. The second [242]Pu peak can be attributed to the migration of Pu(V). The [238]Pu breakthrough includes only one peak that is coincident with the second [242]Pu peak. Interestingly, the difference in [238]Pu and [242]Pu transport could be accounted for by the difference in Pu

oxidation state. The relatively poor fit in the tailing of both ^{242}Pu and ^{238}Pu is likely due to the slow reduction of Pu(V) to Pu(IV) which was not included in the model. Importantly, the deposition of Pu(IV) primarily in the first ~50 μm of the matrix (Figure 4.5 and Figure 4.7) is consistent with the ^{242}Pu depth profiling data shown in Section 3 (note that ^{242}Pu is predominantly Pu(IV)).

Two separate ^{242}Pu breakthrough peaks are not observed in LCA-6. In this case Pu(V) (i.e. ^{238}Pu) is not retarded sufficiently to shift its breakthrough. Nevertheless, ^{242}Pu breakthrough is significantly greater and can be attributed to the contribution of Pu(IV) colloid-facilitated transport.
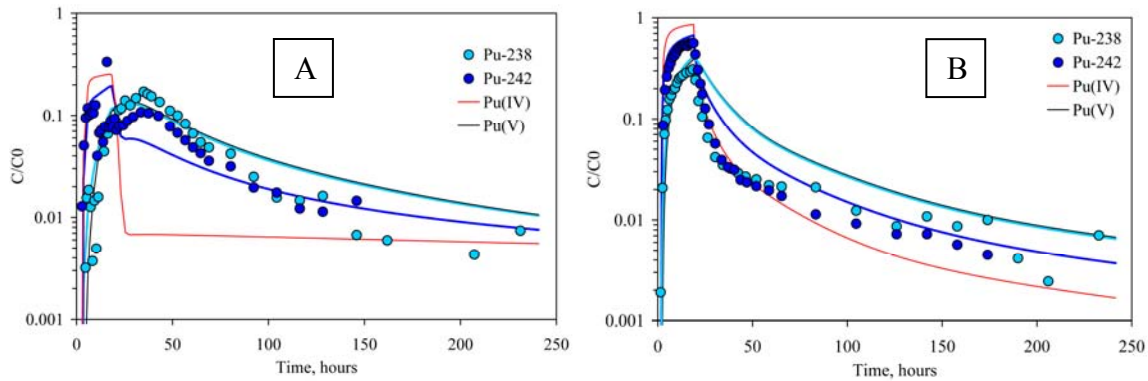
Figure 4.6 Model fits to LCA-5 (A) and LCA-6 (B) Pu elution data. Model results also include transport behavior of Pu(IV) and Pu(V).
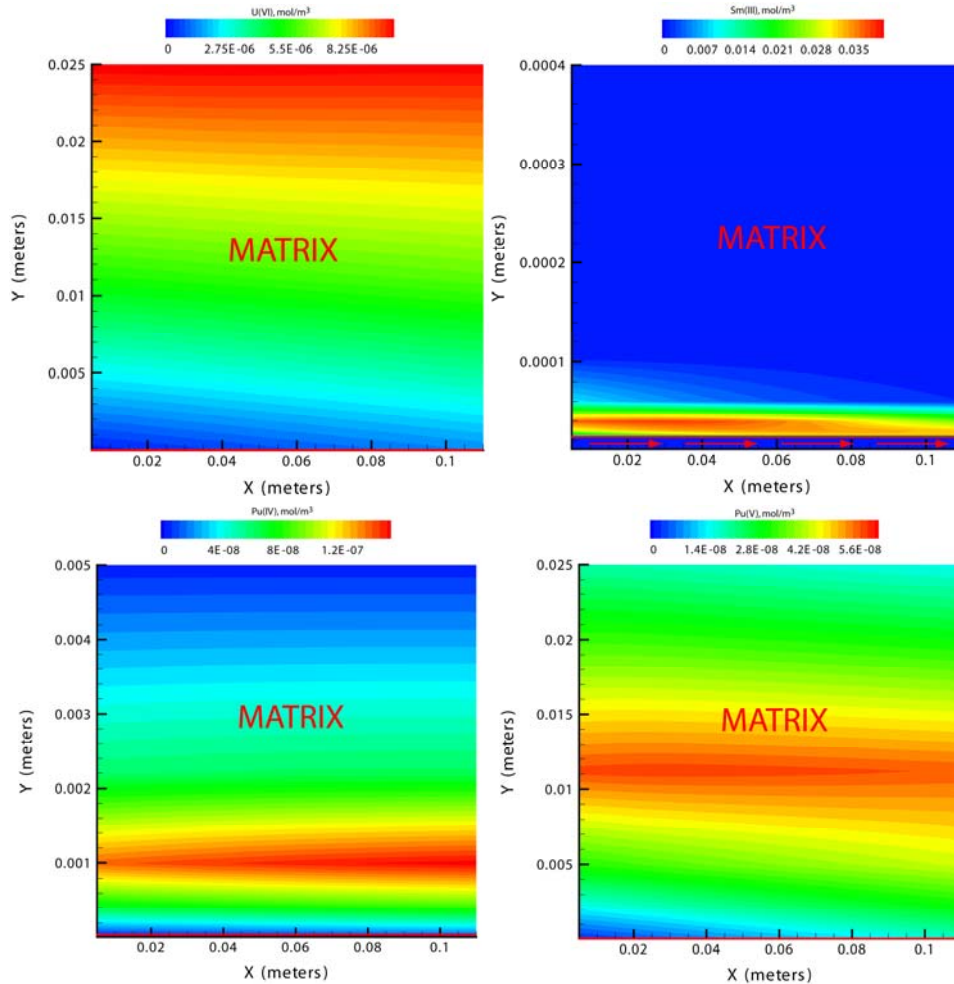
Figure 4.7 LCA-6 model of sorbed radionuclide distribution at end of flowthrough experiment.

5   CONCLUSIONS AND RECOMMENDATIONS

Based on the experimental results and modeling described in this report:

- ^{3}H and Re behave as tracers that diffuse into the rock matrix at rates proportional to their diffusivities in water (Re<^{3}H). High predicted tortuosity values may have resulted from underestimates of porosity.

- U breakthrough was retarded only slightly, indicating a low sorption potential of this radionuclide in carbonate rock.

- Sm migration in carbonate fractures was only observed as a result of colloid-facilitated transport. Thus, in the absence of colloids, Sm transport is unlikely. Based on their analogous reaction chemistry, it is likely that the transport of any of the trivalent rare earth radionuclides (as well as the Am(III) and Cm(III) actinides) will be attributable to colloid-facilitated transport.

- Pu transport in carbonate fractures may occur in the absence of colloids. However, it is likely that this transport is attributable to Pu(V). In the presence of mineral surfaces, Pu

will tend to reduce to Pu(IV) over time. Pu(IV) is unlikely to migrate as a free aqueous species in carbonate fractures. However, it can migrate by colloid-facilitated transport.

- The measured and simulated breakthrough curves show good agreement lending some confidence to the identification of the most significant processes, the performance of high quality and controlled experiments, and the interpretation approach and model being appropriate.

6 ACKNOWLEDGEMENTS

7 REFERENCES

American Petroleum Institute Recommended Practice (API RP) 27 (1952). *Recommended Practice for Determining Permeability of Porous Media*. American Petroleum Institute, Dallas, Texas, 3rd Ed.

American Petroleum Institute Recommended Practice (API RP) 40 (1960). *Recommended Practice for Core Analysis Procedure*. American Petroleum Institute, Dallas, Texas, 1st Ed.

Cartwright, B. G., E. K. Shirk and P. B. Price (1978). "A Nuclear-Track-Recording Polymer of Unique Sensitivity and Resolution." Nuclear Instruments and Methods **153**: 457-460.

Ghazi, A. M., S. Shuttleworth, S. J. Angulo and D. H. Pashley (2000). "New applications for laser ablation high resolution ICPMS (LA-HR-ICP-MS): Quantitative measurements of gallium diffusion across human root dentin." J. Anal. At. Spectrom. **15**: 1335-1341.

Hershey, R. L., W. Howcroft and P. W. Reimus (2003) Laboratory Experiments to Evaluate Diffusion of 14C into Nevada National Security Site Carbonate Aquifer Matrix, Publication No. 45180, Desert Research Institute, Las Vegas, Nevada.

Kemper, W. D. (1986). Solute Diffusivity. Methods of Soil Analysis, Part 1 - Physical and Mineralogical Methods. A. Klute. Madison, Wisconsin, American Society of Agronomy, Inc. and Soil Science Society of America, Inc.

Kersting, A. B., D. W. Efurd, D. L. Finnegan, D. J. Rokop, D. K. Smith and J. L. Thompson (1999). "Migration of plutonium in ground water at the Nevada Test Site." Nature **397**(6714): 56-59.

Kersting, A. B., P. Zhao, M. Zavarin, E. R. Sylwester, Patrick G. Allen, L. Wang, E. J. Nelson and R. W. Williams (2003). Sorption of Pu(IV) on Mineral Colloids. Colloid-Facilitated Transport of Low-solubility Radionuclides: A Field, Experimental, and Modeling Investigation. A. B. Kersting and P. W. Reimus. Livermore, California, Lawrence Livermore National Laboratory**:** UCRL-ID-149688.

Lide, D. R. (2000). CRC Handbook of Chemistry and Physics. Boca Raton, Florida, CRC Press.

Mills, R. 1973. Self-Diffusion in Normal and Heavy Water in the Range 1 - 45°, The Journal of Physical Chemistry, Vol. 77, No. 5, p. 685-688.

Powell, B. A., M. C. Duff, D. I. Kaplan, R. A. Fjeld, M. Newville, D. B. Hunter, P. M. Bertsch, J. T. Coates, P. Eng, M. L. Rivers, S. R. Sutton, I. R. Triay and D. T. Vaniman (2006). "Plutonium oxidation and subsequent reduction by Mn(IV) minerals in Yucca Mountain tuff." Environmental Science & Technology **40**(11): 3508-3514.

Reimus, P. W., S. D. Ware, F. C. Benedict, R. G. Warren, A. Humphrey, A. Adams, B. Wilson and D. Gonzales (2002) Diffusive and Advective Transport of 3H, 14C, and 99Tc in Saturated, Fractured Volcanic Rocks from Pahute Mesa, Nevada, LA-13891-MS, Los Alamos National Laboratory, Los Alamos.

Reimus, P., M. Haga, A. R. Humphrey, D. A. Counce, T. J. Callahan and S. D. Ware (2002). Diffusion Cell and Fracture Transport Experiments to Support Interpretations of the Bullion Forced Gradient Experiment, LA-UR-02-6884, Los Alamos National Laboratory, Los Alamos, New Mexico.

Reimus, P., G. Pohll, T. Mihevc, J. Chapman, M. Haga, B. Lyles, S. Kosinski, R. Niswonger and P. Sanders (2003). "Testing and parameterizing a conceptual model for solute transport in a fractured granite using multiple tracers in a forced gradient test." Water Resources Research **39**(12).

Reimus, P. W. and M. J. Haga (1999). Analysis of tracer responses in the Bullion forced-gradient experiment at Pahute Mesa, Nevada, LA-13615-MS, Los Alamos National Laboratory, Los Alamos, New Mexico.

Russo, R. E., X. L. Mao, O. V. Borisov and H. C. Liu (2000). Laser ablation in atomic spectroscopy. Encyclopedia of Analytical Chemistry: Instrumentation and Applications. R. A. Meyers. Chichster, John Wiley & Sons Ltd**:** 9485-9506.

Russo, R. E., X. L. Mao, H. C. Liu, J. Gonzalez and S. S. Mao (2002). "Laser ablation in analytical chemistry - A review." Talanta **57**(3): 425-451.

Steefel, C. I. and S. B. Yabusaki (1995) OS3D/GIMRT, Software for modeling multicomponent-multidimensional reactive transport, User manual and programmer's guide Richland, WA, Pacific Northwest National Laboratory.

Stoller-Navarro (2004) Geochem04.mdb and A User's Guide to the Comprehensive Water Quality Database for Groundwater in the Vicinity of the Nevada Test Site Las Vegas, Nevada, DOE-NNSA.

Ware, S. D., A. Abdel-Fattah, M. Ding, P. W. Reimus, C. Sedlacek, M. Haga, E. Garcia and S. Chipera (2005) Radionuclide Sorption and Transport in the Lower Carbonate Aquifer and Tuff Confining Unit of Yucca Flat, Nevada Test Site, draft report, Los Alamos National Laboratory, Los Alamos, New Mexico.

Zavarin, M. and C. J. Bruton (2004a) A Non-Electrostatic Surface Complexation Approach to Modeling Radionuclide Migration at the Nevada Test Site: Aluminosilicates, UCRL-TR-208672, Lawrence Livermore National Laboratory, Livermore.

Zavarin, M. and C. J. Bruton (2004b) A Non-Electrostatic Surface Complexation Approach to Modeling Radionuclide Migration at the Nevada Test Site: Iron Oxides and Calcite, UCRL-TR-208673, Lawrence Livermore National Laboratory, Livermore.

Zavarin, M., S. F. Carle and R. M. Maxwell (2004) Upscaling Radionuclide Retardation - Linking the Surface Complexation and Ion Exchange Mechanistic Approach to a Linear Kd Approach, UCRL-TR-204713, Lawrence Livermore National Laboratory, Livermore, California.

Zavarin, M., M. R. Johnson, S. K. Roberts, R. Pletcher, T. P. Rose, A. B. Kersting, G. Eaton, Q. Hu, E. Ramon, J. Walensky and P. Zhao (2005) Radionuclide Transport in Tuff and Carbonate Fractures from Yucca Flat, Nevada Test Site, UCRL-TR-219836, Lawrence Livermore National Laboratory, Livermore, California.

Zavarin, M., S. K. Roberts, P. W. Reimus and M. R. Johnson (2006) Summary of Radionuclide Reactive Transport Experiments in Fractured Tuff and Carbonate Rocks from Yucca Flat, Nevada Test Site, draft report, Lawrence Livermore National Laboratory, Livermore, California.

Zavarin, M., S. K. Roberts, T. P. Rose and D. L. Phinney (2002) Validating Mechanistic Sorption Model Parameters and Processes for Reactive Transport in Alluvium, UCRL-ID-149728, Lawrence Livermore National Laboratory, Livermore, California.

Zavarin, M., S. K. Roberts, N. Hakem, A. Kersting, and A. M. Sawvel. 2005. Eu(III), Sm(III), Np(V), Pu(V), and Pu(IV) sorption to calcite, Radiochimica Acta, 93: 93-102

8   APPENDIX

Table A.1 LCA-5 run parameters.

Well = ER 6-1, core depth = 2601.7-2602.8
Fracture aperture = 500 microns
LCA-5 core mineralogy = 98.4% dolomite and 1.6% calcite
Porosity: 0.967%, Permeability: 1.9×10^{-3} md, Bulk density: 2.80 g/cm^3
Sorption solution of NaHCO$_3$,Mg,K,Ca,^{3}H,Sm,Re, U, Pu
Experiment started on : 21 March 06 08:00
Start pumping sorption solution at: 28 March 06 16:00
Stopped pumping sorption solution at: 29 March 06 07:22
Pump and tubing volume (mL): 2.01

Table A.2 LCA-5 data: Radionuclides and pH.

Sample #	Sampling Time	^{3}H	Pu	Sm	Re	U	Pu	pH
					C/ C$_0$			
	days	LSC			ICP-MS			
3	0.08	-	-	-	-	4.58×10-5	-	-
5	0.11	1.21×10^{-3}	-3.88×10^{-4}	-	-	-	-	-
6	0.12	-	-	1.65×10^{-2}	-	7.50×10^{-5}	1.28×10^{-2}	8.39
8	0.15	6.93×10^{-2}	2.91×10^{-4}	-	-	-	-	-
9	0.16	-	-	7.81×10^{-2}	3.47×10^{-1}	2.58×10^{-4}	5.05×10^{-2}	-
11	0.19	6.26×10^{-1}	3.20×10^{-3}	-	-	-	-	-
12	0.20	-	-	1.19×10^{-1}	8.28×10^{-1}	7.00×10^{-3}	9.47×10^{-2}	-
13	0.22	7.15×10^{-1}	1.55×10^{-2}	-	-	-	-	-
15	0.24	-	-	1.37×10^{-1}	9.50×10^{-1}	3.83×10^{-2}	1.18×10^{-1}	-
16	0.26	8.35×10^{-1}	1.86×10^{-2}	-	-	-	-	8.29
18	0.28	-	-	1.20×10^{-1}	9.60×10^{-1}	9.75×10^{-2}	1.01×10^{-1}	-
19	0.31	8.65×10^{-1}	1.26×10^{-2}	-	-	-	-	-
21	0.33	-	-	1.23×10^{-1}	9.81×10^{-1}	1.74×10^{-1}	1.07×10^{-1}	-
22	0.35	8.89×10^{-1}	3.73×10^{-3}	-	-	-	-	-
24	0.37	-	-	1.22×10^{-1}	9.81×10^{-1}	2.37×10^{-1}	1.05×10^{-1}	-
25	0.39	9.08×10^{-1}	1.46×10^{-2}	-	-	-	-	8.40
27	0.41	-	-	1.36×10^{-1}	9.97×10^{-1}	2.96×10^{-1}	1.26×10^{-1}	-
28	0.43	8.62×10^{-1}	4.94×10^{-3}	-	-	-	-	-
30	0.45	-	-	4.95×10^{-2}	9.87×10^{-1}	3.34×10^{-1}	4.00×10^{-2}	-
31	0.47	9.14×10^{-1}	1.58×10^{-2}	-	-	-	-	-
33	0.49	-	-	7.17×10^{-2}	1.01	3.78×10^{-1}	6.74×10^{-2}	-
36	0.53	-	-	7.24×10^{-2}	1.00	4.10×10^{-1}	7.16×10^{-2}	8.40
39	0.58	-	-	4.52×10^{-2}	1.00	4.31×10^{-1}	5.47×10^{-2}	-
40	0.60	9.05×10^{-1}	4.42×10^{-2}	-	-	-	-	-
42	0.62	-	-	6.02×10^{-2}	9.87×10^{-1}	4.39×10^{-1}	7.79×10^{-2}	-
45	0.66	-	-	3.10×10^{-1}	1.07	4.83×10^{-1}	3.35×10^{-1}	-
46	0.68	9.14×10^{-1}	6.60×10^{-2}	-	-	-	-	8.42
48	0.70	-	-	3.87×10^{-2}	1.05	4.77×10^{-1}	7.58×10^{-2}	-
51	0.74	-	-	4.44×10^{-2}	1.06	4.83×10^{-1}	8.84×10^{-2}	-

Table A.2 (continued).

Sample #	Sampling Time	^{3}H	Pu	Sm	Re	U	Pu	pH
					C/C_0			
	days		LSC			ICP-MS		
53	0.78	9.01×10^{-1}	8.19×10^{-2}	-	-	-	-	-
54	0.78	-	-	2.94×10^{-2}	1.04	4.68×10^{-1}	7.58×10^{-2}	-
56	0.82	8.92×10^{-1}	9.10×10^{-2}	-	-	-	-	-
57	0.83	-	-	3.87×10^{-2}	1.04	4.67×10^{-1}	9.26×10^{-2}	-
59	0.86	9.01×10^{-1}	8.66×10^{-2}	-	-	-	-	-
60	0.87	-	-	2.77×10^{-2}	9.50×10^{-1}	4.25×10^{-1}	7.16×10^{-2}	-
62	0.92	6.06×10^{-1}	1.13×10^{-1}	-	-	-	-	8.46
63	0.93	-	-	1.51×10^{-2}	3.67×10^{-1}	4.09×10^{-1}	7.79×10^{-2}	-
64	0.97	2.76×10^{-1}	1.18×10^{-1}	-	-	-	-	-
66	1.01	-	-	6.88×10^{-3}	1.43×10^{-1}	3.35×10^{-1}	8.00×10^{-2}	-
67	1.06	1.46×10^{-1}	1.40×10^{-1}	-	-	-	-	-
69	1.10	-	-	8.96×10^{-3}	1.06×10^{-1}	2.52×10^{-1}	8.84×10^{-2}	-
70	1.17	7.85×10^{-2}	1.26×10^{-1}	-	-	-	-	-
72	1.23	-	-	6.31×10^{-3}	8.97×10^{-2}	1.47×10^{-1}	9.68×10^{-2}	-
73	1.29	1.38×10^{-1}	1.48×10^{-1}	-	-	-	-	-
76	1.40	-	-	4.37×10^{-3}	1.36×10^{-1}	1.24×10^{-1}	1.07×10^{-1}	8.38
77	1.46	1.31×10^{-1}	1.71×10^{-1}	-	-	-	-	-
79	1.54	9.55×10^{-2}	1.63×10^{-1}	-	-	-	-	-
80	1.56	-	-	4.16×10^{-3}	5.36×10^{-2}	9.25×10^{-2}	1.05×10^{-1}	-
81	1.63	5.94×10^{-2}	1.55×10^{-1}	-	-	-	-	-
84	1.78	-	-	8.96×10^{-3}	8.75×10^{-2}	6.17×10^{-2}	9.89×10^{-2}	-
85	1.81	8.36×10^{-2}	1.36×10^{-1}	-	-	-	-	-
89	2.03	6.42×10^{-2}	1.11×10^{-1}	6.81×10^{-3}	7.11×10^{-2}	5.01×10^{-2}	7.79×10^{-2}	8.54
92	2.19	5.65×10^{-2}	9.96×10^{-2}	6.67×10^{-3}	6.37×10^{-2}	4.71×10^{-2}	6.74×10^{-2}	-
95	2.36	4.97×10^{-2}	8.26×10^{-2}	6.45×10^{-3}	5.94×10^{-2}	5.93×10^{-2}	5.68×10^{-2}	-
98	2.53	3.69×10^{-2}	6.64×10^{-2}	5.73×10^{-3}	4.24×10^{-2}	5.25×10^{-2}	4.84×10^{-2}	-
101	2.69	3.06×10^{-2}	5.44×10^{-2}	5.59×10^{-3}	3.34×10^{-2}	3.89×10^{-2}	4.25×10^{-2}	-
104	2.88	2.56×10^{-2}	4.83×10^{-2}	6.38×10^{-3}	2.71×10^{-2}	3.09×10^{-2}	3.58×10^{-2}	8.48
110	3.35	3.11×10^{-2}	4.19×10^{-2}	5.59×10^{-3}	4.08×10^{-2}	3.33×10^{-2}	3.16×10^{-2}	-
116	3.85	1.30×10^{-2}	2.49×10^{-2}	4.95×10^{-3}	1.45×10^{-2}	1.40×10^{-2}	1.96×10^{-2}	-
122	4.35	1.18×10^{-2}	1.56×10^{-2}	4.44×10^{-3}	1.75×10^{-2}	2.85×10^{-2}	1.75×10^{-2}	-
128	4.85	8.66×10^{-3}	1.47×10^{-2}	4.95×10^{-3}	1.03×10^{-2}	2.08×10^{-2}	1.22×10^{-2}	-
134	5.35	8.66×10^{-3}	1.62×10^{-2}	9.25×10^{-3}	1.86×10^{-2}	1.93×10^{-2}	1.14×10^{-2}	-
143	6.08	1.26×10^{-2}	6.73×10^{-3}	1.49×10^{-2}	1.52×10^{-2}	2.04×10^{-2}	1.45×10^{-2}	-
149	6.75	1.08×10^{-2}	5.96×10^{-3}	5.09×10^{-3}	1.75×10^{-2}	2.78×10^{-2}	-	-
155	7.41	1.82×10^{-3}	3.88×10^{-4}	4.09×10^{-3}	2.28×10^{-3}	1.88×10^{-2}	-	-
161	8.08	1.35×10^{-3}	$^{-2}.42\times10^{-4}$	3.94×10^{-3}	1.64×10^{-3}	1.43×10^{-2}	-	-
166	8.64	2.34×10^{-3}	4.31×10^{-3}	4.30×10^{-3}	2.33×10^{-3}	1.03×10^{-2}	-	-
172	9.30	1.12×10^{-3}	-8.72×10^{-4}	3.87×10^{-3}	1.22×10^{-3}	7.33×10^{-3}	-	-
175	9.64	1.20×10^{-3}	7.41×10^{-3}	3.94×10^{-3}	1.01×10^{-3}	6.75×10^{-3}	-	-
C_0 Values*		3.88×10^{2}	2.06×10^{2}	1.40×10^{2}	1.89×10^{2}	1.20×10^{3}	4.75×10^{-1}	-

* C_0 values for LSC are in counts/ min; C_0 values for ICP-MS are in ng/mL.

Table A.3 LCA-5 data: Major cations.

Sample #	Sampling Time days	Na	Mg	K	Ca
		----------------------		C/C_0	----------------------
3	0.13	7.39×10^{-1}	1.06	7.44×10^{-1}	1.26
6	0.25	7.50×10^{-1}	4.99×10^{-2}	1.69×10^{-2}	5.85×10^{-3}
9	0.38	8.55×10^{-1}	9.07×10^{-2}	2.82×10^{-2}	9.76×10^{-3}
12	0.50	9.77×10^{-1}	6.35×10^{-2}	2.25×10^{-2}	6.50×10^{-3}
15	0.63	1.02	6.35×10^{-2}	1.69×10^{-2}	6.50×10^{-3}
18	0.75	9.88×10^{-1}	4.54×10^{-2}	1.13×10^{-2}	5.20×10^{-3}
21	0.88	9.89×10^{-1}	8.62×10^{-2}	2.82×10^{-2}	9.76×10^{-3}
24	1.00	9.83×10^{-1}	4.08×10^{-2}	1.13×10^{-2}	2.93×10^{-3}
27	1.13	9.90×10^{-1}	4.99×10^{-2}	1.69×10^{-2}	6.50×10^{-3}
30	1.25	9.87×10^{-1}	8.16×10^{-2}	2.25×10^{-2}	9.76×10^{-3}
33	1.38	1.01	6.35×10^{-2}	2.25×10^{-2}	6.50×10^{-3}
36	1.50	1.00	3.17×10^{-2}	7.89×10^{-3}	3.90×10^{-3}
39	1.63	1.00	9.07×10^{-2}	2.82×10^{-2}	1.30×10^{-2}
42	1.75	9.90×10^{-1}	6.35×10^{-2}	1.69×10^{-2}	6.50×10^{-3}
48	2.00	1.05	6.80×10^{-2}	1.69×10^{-2}	9.76×10^{-3}
51	2.13	1.07	4.08×10^{-2}	1.13×10^{-2}	5.85×10^{-3}
54	2.25	1.06	3.63×10^{-2}	1.69×10^{-2}	5.85×10^{-3}
57	2.38	1.06	6.80×10^{-2}	1.69×10^{-2}	5.85×10^{-3}
60	2.50	9.87×10^{-1}	8.62×10^{-2}	2.25×10^{-2}	9.76×10^{-3}
63	2.63	8.61×10^{-1}	3.63×10^{-2}	1.69×10^{-2}	5.53×10^{-3}
66	2.75	7.80×10^{-1}	6.80×10^{-2}	2.82×10^{-2}	9.76×10^{-3}
69	2.88	7.54×10^{-1}	4.08×10^{-2}	1.13×10^{-2}	5.85×10^{-3}
72	3.00	7.57×10^{-1}	3.17×10^{-2}	1.69×10^{-2}	4.55×10^{-3}
76	3.17	7.34×10^{-1}	3.17×10^{-2}	1.01×10^{-2}	3.90×10^{-3}
80	3.33	7.35×10^{-1}	6.35×10^{-2}	2.82×10^{-2}	9.76×10^{-3}
84	3.50	7.48×10^{-1}	4.08×10^{-2}	1.13×10^{-2}	4.88×10^{-3}
89	3.71	7.89×10^{-1}	6.35×10^{-2}	2.82×10^{-2}	9.76×10^{-3}
92	3.83	7.77×10^{-1}	4.08×10^{-2}	1.69×10^{-2}	5.53×10^{-3}
95	3.96	7.67×10^{-1}	4.54×10^{-2}	1.69×10^{-2}	5.53×10^{-3}
98	4.08	7.59×10^{-1}	7.71×10^{-2}	3.38×10^{-2}	9.76×10^{-3}
101	4.21	7.49×10^{-1}	8.16×10^{-2}	3.38×10^{-2}	9.76×10^{-3}
104	4.33	7.41×10^{-1}	2.72×10^{-2}	8.45×10^{-3}	3.25×10^{-3}
110	4.58	7.77×10^{-1}	4.54×10^{-2}	2.25×10^{-2}	6.50×10^{-3}
116	4.83	7.65×10^{-1}	8.16×10^{-2}	3.38×10^{-2}	9.76×10^{-3}
122	5.08	8.18×10^{-1}	6.80×10^{-2}	2.25×10^{-2}	9.76×10^{-3}
128	5.33	7.70×10^{-1}	4.99×10^{-2}	1.69×10^{-2}	6.50×10^{-3}
134	5.58	7.87×10^{-1}	7.26×10^{-2}	3.38×10^{-2}	9.76×10^{-3}
143	5.96	7.81×10^{-1}	5.44×10^{-2}	2.25×10^{-2}	6.50×10^{-3}
149	6.21	7.74×10^{-1}	3.17×10^{-2}	1.69×10^{-2}	5.85×10^{-3}
155	6.46	7.75×10^{-1}	5.44×10^{-2}	2.25×10^{-2}	6.50×10^{-3}
161	6.71	7.82×10^{-1}	4.99×10^{-2}	2.25×10^{-2}	4.88×10^{-3}
166	6.92	9.36×10^{-1}	6.35×10^{-2}	2.25×10^{-2}	9.76×10^{-3}
172	7.17	7.86×10^{-1}	5.44×10^{-2}	2.25×10^{-2}	9.76×10^{-3}
175	7.29	7.68×10^{-1}	4.54×10^{-2}	1.69×10^{-2}	6.18×10^{-3}
C_0 Values		$\mathbf{9.47\times10^{4}}$	$\mathbf{2.21\times10^{4}}$	$\mathbf{1.78\times10^{4}}$	$\mathbf{3.08\times10^{4}}$

* C_0 values for ICP-MS are in ng/mL.

Table A.4 LCA-6 run parameters.

Well = ER 6-1, core depth = 2619.0-2620.0
Fracture aperture = 50 microns
LCA-6 core mineralogy = 100% dolomite
Porosity: 4.894%, Permeability: 6.0 m/d, Bulk density: 2.70 g/cm^3
Sorption solution of $NaHCO_3$,Mg,K,Ca,^{3}H,Sm,Re, U,Pu
Experiment started on: 28 June 06 10:00
Start pumping sorption solution at: 11 July 06 14:56
Stopped pumping sorption solution at: 12 July 06 07:47
Pump and tubing volume (mL): 2.521 mL

Table A.5 LCA-6 data: Radionuclides and pH.

Sample #	Sampling Time	^{3}H	Pu	Sm	Re	U	Pu	pH
				---- C/C_0 ----				
	days	---- LSC ----		---- ICP-MS ----				
5	0.06	2.50×10^{-4}	1.90×10^{-3}	-	-	-	-	-
8	0.10	3.28×10^{-3}	2.08×10^{-2}	-	-	-	-	7.73
9	0.12	-	-	2.39×10^{-2}	3.28×10^{-2}	1.02×10^{-1}	8.63×10^{-2}	-
11	0.15	9.45×10^{-2}	7.06×10^{-2}	-	-	-	-	-
12	0.16	-	-	3.87×10^{-2}	1.79×10^{-1}	2.39×10^{-1}	1.94×10^{-1}	-
13	0.17	1.63×10^{-1}	9.75×10^{-2}	-	-	-	-	-
15	0.20	-	-	5.62×10^{-2}	3.09×10^{-1}	3.34×10^{-1}	2.63×10^{-1}	-
16	0.22	2.82×10^{-1}	1.24×10^{-1}	-	-	-	-	-
18	0.24	-	-	7.09×10^{-2}	4.12×10^{-1}	4.18×10^{-1}	3.22×10^{-1}	-
19	0.26	3.66×10^{-1}	1.58×10^{-1}	-	-	-	-	-
21	0.28	-	-	8.38×10^{-2}	4.80×10^{-1}	4.74×10^{-1}	3.57×10^{-1}	-
22	0.30	4.36×10^{-1}	1.73×10^{-1}	-	-	-	-	-
24	0.33	-	-	9.48×10^{-2}	5.53×10^{-1}	5.35×10^{-1}	4.06×10^{-1}	7.92
25	0.34	4.80×10^{-1}	1.96×10^{-1}	-	-	-	-	-
27	0.37	-	-	1.03×10^{-1}	5.87×10^{-1}	5.68×10^{-1}	4.24×10^{-1}	-
28	0.38	5.26×10^{-1}	2.03×10^{-1}	-	-	-	-	-
30	0.41	-	-	1.13×10^{-1}	6.40×10^{-1}	6.12×10^{-1}	4.53×10^{-1}	-
31	0.42	5.57×10^{-1}	2.29×10^{-1}	-	-	-	-	-
33	0.45	-	-	1.73×10^{-1}	6.97×10^{-1}	6.73×10^{-1}	4.92×10^{-1}	-
34	0.47	6.20×10^{-1}	2.51×10^{-1}	-	-	-	-	-
36	0.49			1.79×10^{-1}	7.13×10^{-1}	6.90×10^{-1}	5.12×10^{-1}	-
37	0.51	6.50×10^{-1}	2.62×10^{-1}	-	-	-	-	-
39	0.53	-	-	1.61×10^{-1}	7.44×10^{-1}	7.19×10^{-1}	5.24×10^{-1}	-
40	0.55	6.59×10^{-1}	2.70×10^{-1}	-	-	-	-	-
42	0.58	-	-	1.88×10^{-1}	7.51×10^{-1}	7.31×10^{-1}	5.34×10^{-1}	-
45	0.62			1.95×10^{-1}	7.59×10^{-1}	7.37×10^{-1}	5.40×10^{-1}	-
46	0.63	6.98×10^{-1}	2.88×10^{-1}	-	-	-	-	-
48	0.66	-	-	1.98×10^{-1}	7.70×10^{-1}	7.46×10^{-1}	5.28×10^{-1}	-
51	0.70	-	-	2.02×10^{-1}	7.78×10^{-1}	7.54×10^{-1}	5.59×10^{-1}	-
52	0.72	7.09×10^{-1}	2.95×10^{-1}	-	-	-	-	-
54	0.74	-	-	2.13×10^{-1}	7.99×10^{-1}	7.66×10^{-1}	5.61×10^{-1}	-
56	0.77	7.18×10^{-1}	3.10×10^{-1}	-	-	-	-	-
57	0.78	-	-	2.02×10^{-1}	7.97×10^{-1}	7.61×10^{-1}	5.63×10^{-1}	-

Table A.5 (continued).

Sample #	Sampling Time	^{3}H	Pu	Sm	Re	U	Pu	pH
					C/C_0			
	days	LSC			ICP-MS			
60	0.83	6.74×10^{-1}	2.44×10^{-1}	1.52×10^{-1}	7.28×10^{-1}	5.97×10^{-1}	4.36×10^{-1}	-
63	0.88	-	-	1.17×10^{-1}	5.59×10^{-1}	4.41×10^{-1}	3.06×10^{-1}	-
64	0.90	4.86×10^{-1}	1.51×10^{-1}	-	-	-	-	-
66	0.94	-	-	8.38×10^{-2}	4.18×10^{-1}	3.24×10^{-1}	2.24×10^{-1}	-
69	0.98	3.34×10^{-1}	1.06×10^{-1}	6.81×10^{-2}	3.40×10^{-1}	2.67×10^{-1}	1.77×10^{-1}	-
72	1.04	-	-	5.34×10^{-2}	2.39×10^{-1}	1.92×10^{-1}	1.28×10^{-1}	-
74	1.10	1.95×10^{-1}	6.49×10^{-2}	-	-	-	-	-
75	1.13	-	-	3.77×10^{-2}	1.81×10^{-1}	1.36×10^{-1}	8.83×10^{-2}	7.90
80	1.26	1.24×10^{-1}	4.18×10^{-2}	2.58×10^{-2}	1.21×10^{-1}	8.92×10^{-2}	5.69×10^{-2}	-
85	1.40	-	-	2.12×10^{-2}	8.79×10^{-2}	6.47×10^{-2}	3.92×10^{-2}	-
86	1.43	8.84×10^{-2}	3.49×10^{-2}	-	-	-	-	-
90	1.54	-	-	1.66×10^{-2}	7.18×10^{-2}	5.26×10^{-2}	3.34×10^{-2}	7.91
92	1.60	6.72×10^{-2}	3.22×10^{-2}	-	-	-	-	-
95	1.68	-	-	1.66×10^{-2}	6.03×10^{-2}	4.64×10^{-2}	3.14×10^{-2}	7.87
98	1.76	5.76×10^{-2}	2.92×10^{-2}	-	-	-	-	-
100	1.82	-	-	1.20×10^{-2}	5.36×10^{-2}	4.15×10^{-2}	2.49×10^{-2}	7.90
104	1.93	5.38×10^{-2}	2.68×10^{-2}	-	-	-	-	-
105	1.96	-	-	1.01×10^{-2}	4.89×10^{-2}	3.65×10^{-2}	2.35×10^{-2}	-
110	2.17	3.98×10^{-2}	2.52×10^{-2}	1.01×10^{-2}	3.90×10^{-2}	3.15×10^{-2}	2.16×10^{-2}	-
115	2.44	3.39×10^{-2}	2.21×10^{-2}	8.28×10^{-3}	3.48×10^{-2}	2.70×10^{-2}	1.96×10^{-2}	-
120	2.72	2.87×10^{-2}	2.14×10^{-2}	6.44×10^{-3}	2.86×10^{-2}	2.41×10^{-2}	1.73×10^{-2}	8.15
128	3.47	1.73×10^{-2}	2.11×10^{-2}	-	1.82×10^{-2}	1.79×10^{-2}	1.14×10^{-2}	-
136	4.36	9.87×10^{-3}	1.24×10^{-2}	-	1.14×10^{-2}	1.33×10^{-2}	9.22×10^{-3}	8.17
144	5.25	7.90×10^{-3}	8.68×10^{-3}	-	9.88×10^{-3}	1.05×10^{-2}	7.26×10^{-3}	8.24
150	5.92	8.38×10^{-3}	1.09×10^{-2}	-	1.14×10^{-2}	1.07×10^{-2}	7.26×10^{-3}	-
156	6.58	6.40×10^{-3}	8.68×10^{-3}	-	7.80×10^{-3}	8.13×10^{-3}	5.69×10^{-3}	8.07
162	7.25	3.45×10^{-3}	1.00×10^{-2}	-	5.72×10^{-3}	6.22×10^{-3}	4.51×10^{-3}	-
168	7.92	2.53×10^{-3}	4.16×10^{-3}	-	4.16×10^{-3}	5.89×10^{-3}	-	-
174	8.58	2.27×10^{-3}	2.45×10^{-3}	-	3.64×10^{-3}	4.98×10^{-3}	-	8.13
179	9.14	5.46×10^{-4}	-1.25×10^{-3}	-	3.12×10^{-3}	-	-	-
184	9.69	1.18×10^{-3}	7.06×10^{-3}	-	2.60×10^{-3}	-	-	8.06
C_0 Values*		3.48×10^2	2.15×10^2	1.09×10^2	1.92×10^2	1.21×10^3	5.10×10^{-1}	-

* C_0 values for LSC are in counts/ min; C_0 values for ICP-MS are in ng/mL.

Table A.6 LCA-6 data: Major cations.

Sample #	Sampling Time	Na	Mg	K	Ca
	days	----------------------		C/C$_0$	----------------------
6	0.08	0.64	1.12	0.14	1.59
9	0.12	0.66	1.14	0.14	1.54
12	0.16	0.64	1.07	0.17	1.35
15	0.20	0.75	1.21	0.27	1.55
18	0.24	0.78	1.25	0.35	1.50
21	0.28	0.80	1.23	0.40	1.51
24	0.33	0.83	1.25	0.46	1.52
27	0.37	0.85	1.25	0.51	1.58
30	0.41	0.87	1.28	0.56	1.58
33	0.45	0.88	1.18	0.67	1.44
36	0.49	0.88	1.17	0.67	1.43
39	0.53	0.90	1.18	0.70	1.49
42	0.58	0.90	1.21	0.71	1.45
45	0.62	0.89	1.18	0.72	1.48
48	0.66	0.90	1.19	0.74	1.44
51	0.70	0.89	1.17	0.74	1.46
54	0.74	0.93	1.22	0.76	1.49
57	0.78	0.92	1.20	0.75	1.45
60	0.83	0.90	1.17	0.73	1.43
63	0.88	0.88	1.17	0.66	1.41
66	0.94	0.84	1.13	0.54	1.41
69	0.98	0.83	1.14	0.47	1.32
72	1.04	0.82	1.11	0.40	1.26
75	1.13	0.82	1.12	0.35	1.25
80	1.26	0.81	1.12	0.30	1.28
85	1.40	0.79	1.11	0.26	1.25
90	1.54	0.80	1.14	0.25	1.25
95	1.68	0.79	1.12	0.23	1.28
100	1.82	0.80	1.15	0.23	1.31
105	1.96	0.80	1.16	0.22	1.33
110	2.17	0.81	1.17	0.21	1.34
115	2.44	0.81	1.21	0.21	1.36
120	2.72	0.80	1.19	0.20	1.36
128	3.47	0.81	1.21	0.19	1.36
136	4.36	0.81	1.20	0.18	1.32
144	5.25	0.81	1.18	0.18	1.39
150	5.92	0.81	1.26	0.18	1.44
156	6.58	0.81	1.24	0.18	1.43
162	7.25	0.80	1.18	0.17	1.31
168	7.92	0.81	1.17	0.17	1.20
174	8.58	0.81	1.19	0.17	1.33
179	9.14	0.82	1.19	0.17	1.20
184	9.69	0.85	1.22	0.17	1.22
C$_0$ Values *		**8.45×10^4**	**2.13×10^4**	**8.74×10^4**	**2.15×10^4**

* C$_0$ values for cations are in ng/mL.

Figure A.1 LCA-5 Synthetic parallel plate fracture.

Figure A.2 LCA-6 Synthetic parallel plate fracture.